

# RESULTS FROM A SYSTEMATIC SURVEY OF X-RAY EMISSION FROM HYDROGEN-POOR SUPERLUMINOUS SNE

R. MARGUTTI<sup>1</sup>, R. CHORNOCK<sup>2</sup>, B. D. METZGER<sup>3</sup>, D. L. COPPEJANS<sup>1</sup>, C. GUIDORZI<sup>4</sup>, G. MIGLIORI<sup>5</sup>, D. MILISAVLJEVIC<sup>6</sup>, E. BERGER<sup>6</sup>, M. NICHOLL<sup>6</sup>, B. A. ZAUDERER<sup>7</sup>, R. LUNNAN<sup>8</sup>, A. KAMBLE<sup>6</sup>, M. DROUT<sup>9,10</sup>, M. MODJAZ<sup>7</sup>

Draft version January 13, 2022

## ABSTRACT

We present the results from a sensitive X-ray survey of 26 nearby hydrogen-poor superluminous supernovae (SLSNe-I) with *Swift*, Chandra and XMM. This dataset constrains the SLSN evolution from a few days until  $\sim 2000$  days after explosion, reaching a luminosity  $L_x \sim 10^{40} \text{ erg s}^{-1}$  and revealing the presence of significant X-ray emission at the location of PTF12dam. No SLSN-I is detected above  $L_x \sim 10^{41} \text{ erg s}^{-1}$ , suggesting that the luminous X-ray emission  $L_x \sim 10^{45} \text{ erg s}^{-1}$  associated with SCP60F6 is not common among SLSNe-I. We constrain the presence of off-axis GRB jets, ionization breakouts from magnetar central engines and the density in the sub-pc environments of SLSNe-I through Inverse Compton emission. The deepest limits rule out the weakest uncollimated GRB outflows, suggesting that if the similarity of SLSNe-I with GRB/SNe extends to their fastest ejecta, then SLSNe-I are either powered by energetic jets pointed far away from our line of sight ( $\theta > 30^\circ$ ), or harbor failed jets that do not successfully break through the stellar envelope. Furthermore, if a magnetar central engine is responsible for the exceptional luminosity of SLSNe-I, our X-ray analysis favors large magnetic fields  $B > 2 \times 10^{14} \text{ G}$  and ejecta masses  $M_{ej} > 3 M_\odot$  in agreement with optical/UV studies. Finally, we constrain the pre-explosion mass-loss rate of stellar progenitors of SLSNe-I. For PTF12dam we infer  $\dot{M} < 2 \times 10^{-5} M_\odot \text{ yr}^{-1}$ , suggesting that the SN shock interaction with the CSM is unlikely to supply the main source of energy powering the optical transient and that some SLSN-I progenitors end their life as compact stars surrounded by a low-density medium similar to long GRBs and Type Ib/c SNe.

*Subject headings:* supernovae: specific (SCP06F6, PTF09cnd, SN2010gx, SN2010kd, SN2011ke, SN2012il, PTF12dam, iPTF13ehe, CSS140925-005854, LSQ14fxj, LSQ14mo, LSQ14an, PS1-14bj, DES15S2nr, SN2015bn/PS15ae, SN2016ard, PSQ16aqv)

## 1. INTRODUCTION

Superluminous supernovae (SLSNe) are among the most luminous known stellar explosions in the Universe. Recognized as a class only in 2009 (Quimby et al. 2011c, Chomiuk et al. 2011), SLSNe reach optical-UV luminosities  $L > 7 \times 10^{43} \text{ erg s}^{-1}$ ,  $\sim 10$ – $100$  more luminous than common SNe, and are likely associated with the death of massive stars. The source of energy powering their exceptional energy release is still debated (e.g. Gal-Yam 2012). The proposed energy sources include: (i) radioactive decay of large amounts of freshly synthesized  $^{56}\text{Ni}$  ( $M_{\text{Ni}} \gtrsim 5 M_\odot$ ), a signature of pair-instability explosions (as proposed for SN 2007bi, Gal-Yam et al. 2009); (ii) SN shock interaction with dense material in the environment (e.g. Smith & McCray 2007, Chevalier &

Irwin 2011); (iii) a magnetar central engine (e.g. Kasen & Bildsten 2010; Woosley 2010; Nicholl et al. 2013). The narrow features ( $v \lesssim 100 \text{ km s}^{-1}$ ) in the spectra of hydrogen-rich SLSNe like SN2006gy clearly indicate that the interaction of the SN blast wave with the medium plays a role (e.g. Smith & McCray 2007; Ofek et al. 2007), while it is unclear if a single mechanism can power hydrogen-stripped SLSNe (i.e. SLSNe-I). Indeed, SLSN-I iPTF13ehe has been interpreted as the combination of energy extracted from a magnetar central engine coupled with radiation from the radioactive decay of  $\sim 2.5 M_\odot$  of  $^{56}\text{Ni}$ , and a late-time interaction of the SN shock with the medium (Yan et al. 2015; Wang et al. 2016).

A number of independent lines of evidence support the idea that SLSNe-I might harbor an engine. Observations of SLSN-I host galaxies indicate a preference for low-metallicity environments, which inspired a connection with long Gamma-Ray Bursts (GRBs, Lunnan et al. 2014; Leloudas et al. 2015b; Perley et al. 2016; Chen et al. 2016, see however Angus et al. 2016). Along the same line, Greiner et al. (2015) reported the detection of typical SLSN spectral features in SN2011kl associated with GRB 111209A, and suggested that a magnetar central engine powered both the initial burst of  $\gamma$ -rays and the later optical/UV SN emission (Metzger et al. 2015). Milisavljevic et al. (2013) found links between the late-time emission properties of a subset of energetic, slow-evolving supernovae and the superluminous SN2007bi. They suggested that a single, possibly jetted, explosion mechanism may unify all of these events that span  $-21 \leq M_B \leq -17$  mag. Additionally, nebular spectroscopic studies by Nicholl et al. (2016a) revealed similarities between the SLSN-I 2015bn and SN 1998bw, associated with GRB 980425, suggesting that the cores of their massive progenitors shared a similar structure at

<sup>1</sup> Center for Interdisciplinary Exploration and Research in Astrophysics (CIERA) and Department of Physics and Astronomy, Northwestern University, Evanston, IL 60208

<sup>2</sup> Astrophysical Institute, Department of Physics and Astronomy, 251B Clippinger Lab, Ohio University, Athens, OH 45701, USA

<sup>3</sup> Columbia Astrophysics Laboratory, Columbia University, Pupin Hall, New York, NY 10027, USA

<sup>4</sup> Department of Physics and Earth Science, University of Ferrara, via Saragat 1, I-44122, Ferrara, Italy

<sup>5</sup> Laboratoire AIM (CEA/IRFU - CNRS/INSU - Université Paris Diderot), CEA DSM/SAp, F-91191 Gif-sur-Yvette, France

<sup>6</sup> Harvard-Smithsonian Center for Astrophysics, 60 Garden St., Cambridge, MA 02138, USA

<sup>7</sup> Center for Cosmology and Particle Physics, New York University, 4 Washington Place, New York, NY 10003, USA

<sup>8</sup> Department of Astronomy, California Institute of Technology, 1200 East California Boulevard, Pasadena, CA 91125, USA

<sup>9</sup> Carnegie Observatories, 813 Santa Barbara Street, Pasadena, CA 91101, USA 2

<sup>10</sup> Hubble, Carnegie-Dunlap Fellow

the time of collapse. In another source, SLSN-I Gaia 16apd, Nicholl et al. (2017) further demonstrate that the luminous excess of UV emission originates from a central source of energy, rather than reduced UV absorption or shock interaction with a thick medium (see however Yan et al. 2016). Finally, luminous X-ray emission has been detected at the location of the SLSN-I SCP06F6 (Gänsicke et al. 2009) with luminosity  $L_x \sim 10^{45} \text{ erg s}^{-1} \sim 70$  days (rest-frame) after the explosion (Levan et al. 2013). At this epoch, SCP06F6 even outshines GRBs by a large factor, suggesting the presence of a still-active central engine that manifests itself through very luminous and long-lasting X-ray emission (Levan et al. 2013; Metzger et al. 2015). Before our effort, SCP06F6 was the only SLSN-I for which an X-ray source was detected at a location consistent with the optical transient.

These observational results suggest a connection between SLSNe-I and engine-driven SNe. However, it is not yet known how the properties of the engines (successful jet? relativistic ejecta? collimated or spherical central-engine powered outflow?), progenitor stars, and circumstellar environments would compare. Here we present the results from a systematic search for X-ray emission from SLSNe-I both at early and at late times, which directly depends on the properties of the immediate environment and central engine (if any). The direct detection of the stellar progenitors of SLSNe-I in pre-explosion optical images is not possible due to their large distances ( $z \geq 0.1$ ). Sampling the circumstellar density profile in the closest environment is thus the most direct probe of their progenitors and their recent mass-loss history before stellar death.

The dataset that we present here includes the deepest X-ray observations of SLSNe-I with *Swift*, XMM and the Chandra X-ray Observatory (CXO), extending from the time of discovery until  $\sim 2000$  days (rest-frame) after explosion and led to the discovery of X-ray emission at the location of the slowly evolving SLSN-I PTF12dam. These observations, described in Sec. 2, indicate that superluminous X-ray emission similar to what was observed in association with SCP06F6 is not common in SLSNe-I (Sec. 3) and allow us to place meaningful constraints on the environment density at the SLSN site (Sec. 4). We constrain the properties of central engines in SLSNe-I in Sec. 5 by investigating the presence of late-time X-ray re-brightenings that can either be due to emission from off-axis collimated relativistic outflows similar to GRBs, or to the ionization breakouts from magnetar central engines (Metzger et al. 2014). Conclusions are drawn in Sec. 6.

## 2. X-RAY OBSERVATIONS AND ANALYSIS

Since 2011, we routinely followed up all publicly announced nearby ( $z \lesssim 0.5$ ) SLSNe-I with *Swift*-XRT with a series of observations acquired between the time of discovery and  $\sim 360$  days (rest-frame) after explosion. For a subset of events we acquired deep X-ray observations with dedicated programs on the Chandra X-ray Observatory (CXO) and XMM-Newton. Additionally, we searched the *Swift*-XRT, CXO and XMM archives for serendipitous or unpublished observations of SLSNe-I discovered before May 2016. Our final sample consists of 26 SLSNe-I discovered between 2006 and May 2016. The dataset covers the time range between  $\sim$ days after explosion until  $\sim 2000$  days (rest-frame), and comprises  $\sim 700$  hrs of observations. We update the X-ray observations of the sample of 11 SLSNe-I from Levan et al. (2013) with

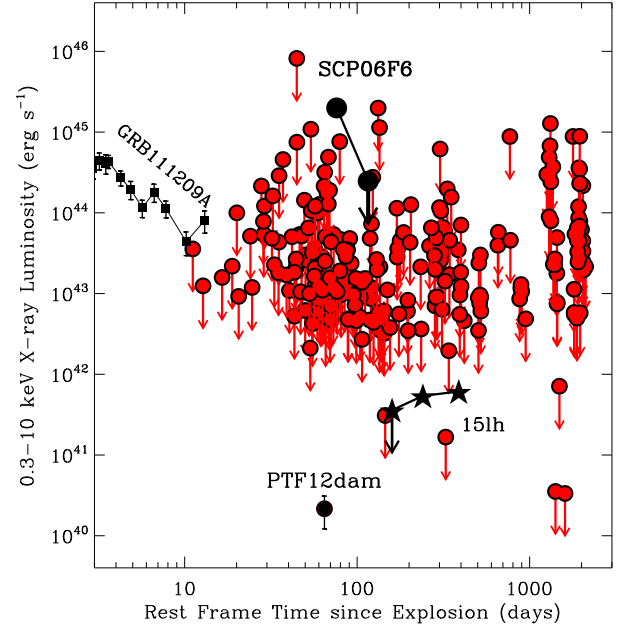


FIG. 1.— X-ray observations of SLSNe-I spanning the time range  $\sim 10$ –2000 days (red circles for upper limits, black circles for detections) show that superluminous X-ray emission of the kind detected at the location of SCP06F6 (Gänsicke et al. 2009, Levan et al. 2013) is not common. Black stars: X-ray emission at the location of ASASSN-15lh (Margutti et al. 2017b), which has a very disputed physical origin. Black squares: X-ray afterglow of GRB 112109A, associated with the over-luminous SN 2011kl (Greiner et al. 2015).

the most recent data<sup>11</sup> and we add 15 new SLSNe-I. Inserra et al. (2017) present a selection of *Swift*-XRT observations of three SLSNe. The much longer temporal baseline and better sensitivity of the X-ray dataset presented here allow us to constrain the environments and the properties of central engines possibly powering the SLSN emission.

We divide our sample into three groups: the “gold sample” (Table 1) contains 4 SLSNe-I with X-ray detections or well sampled optical bolometric light-curve and deep X-ray limits obtained with XMM or the CXO. The “bronze sample” contains 12 SLSNe-I with sparser optical data but with good *Swift*-XRT X-ray coverage (Table 2), while the “iron sample” comprises 10 SLSNe-I with very sparse optical and X-ray data (Table 3). Given the peculiar nature of ASASSN-15lh (Metzger et al. 2015; Dong et al. 2016; Leloudas et al. 2016; van Putten & Della Valle 2016; Chatzopoulos et al. 2016; Dai et al. 2015; Sukhbold & Woosley 2016; Bersten et al. 2016; Kozyreva et al. 2016; Godoy-Rivera et al. 2016; Margutti et al. 2017a), this transient is not part of the sample of bona fide SLSNe-I analyzed here. However, we discuss and compare the X-ray properties of ASASSN-15lh in the context of SLSNe-I in Sec. 4, 5.1 and 5.2.

*Swift*-XRT data have been analyzed using HEASOFT (v6.18) and corresponding calibration files, following standard procedures (see Margutti et al. 2013a for details). For each SLSN-I we provide stacked flux limits (for visualization purposes only), and flux limits derived from individual observations (Table 5 in Appendix A). CXO data have been analyzed with the CIAO software package (v4.9) and correspond-

<sup>11</sup> Note that PTF11dsf and CSS121015, included by Levan et al. (2013) in the sample of SLSNe-I are in fact H-rich events (see Benetti et al. 2014; Perley et al. 2016). Additionally, for PTF11dsf an AGN interpretation cannot be ruled out (Perley et al. 2016). For these reasons, we do not include these two events in our sample of SLSNe-I.

TABLE 1  
GOLD SAMPLE.

SN	z	$d_L$ (Mpc)	Discovery Date (MJD)	Inferred Explosion Date (MJD)	$N_{H,MW}$ ( $10^{20}\text{cm}^{-2}$ )	Instrument
SCP06F6	1.189	8310	53787 <sup>a</sup>	53767 <sup>b</sup>	0.885	XMM+CXO
PTF12dam	0.107	498	56037 <sup>a</sup>	56022 <sup>c</sup>	1.11	Swift+CXO
PS1-14bj	0.521	3012	56618 <sup>d</sup>	56611 <sup>e</sup>	1.71	XMM
SN 2015bn/PS15ae	0.1136	513.2	57014 <sup>f</sup>	57013 <sup>g</sup>	2.37	Swift+XMM

<sup>a</sup>From [Levan et al. \(2013\)](#).<sup>b</sup>The time of peak is MJD 53872. The rise time is  $\sim 50$  days in the rest frame ([Barbary et al. 2009](#)).<sup>c</sup>The light-curve reached maximum light on MJD 56088 and the rest-frame rise-time is  $\sim 60$  days ([Nicholl et al. 2013](#)).<sup>d</sup>From [Lunnan et al. \(2016\)](#).<sup>e</sup>[Lunnan et al. \(2016\)](#) estimate a peak time on MJD 56801.3 and a rest-frame rise-time  $\gtrsim 125$  days.<sup>f</sup>From [Nicholl et al. \(2016a\)](#).<sup>g</sup>The SN reached  $r$ -band maximum light on MJD 57102 ([Nicholl et al. 2016a](#)). The rise-time inferred by [Nicholl et al. \(2016a\)](#) is  $\sim 80$  days in the rest-frame.TABLE 2  
BRONZE SAMPLE.

SN	z	$d_L$ (Mpc)	Discovery Date (MJD)	Inferred Explosion Date (MJD)	$N_{H,MW}$ ( $10^{20}\text{cm}^{-2}$ )	Instrument
PTF09cnd	0.258	1317	55025 <sup>a</sup>	55006 <sup>b</sup>	2.20	Swift+XMM
SN 2010gx	0.230	1156	55260 <sup>a</sup>	55251 <sup>c</sup>	3.28	Swift
SN 2010kd	0.101	468	55453 <sup>a</sup>	55398 <sup>d</sup>	2.32	Swift
SN 2011ke	0.143	682	55650 <sup>a</sup>	55649 <sup>e</sup>	1.27	Swift+CXO
SN 2012il	0.175	851	55926 <sup>a</sup>	55919 <sup>e</sup>	2.38	Swift
iPTF13ehe	0.3434	1833	56621 <sup>f</sup>	56496.4 <sup>g</sup>	4.30	Swift
LSQ14mo	0.253	1288	56687 <sup>h</sup>	56624 <sup>i</sup>	6.59	Swift
LSQ14an	0.163	787	56689 <sup>j</sup>	56513 <sup>j</sup>	6.13	Swift
CSS140925-005854	0.46	2590	56920 <sup>k</sup>	56900 <sup>k</sup>	3.99	Swift
LSQ14fxj	0.36	1937	56942 <sup>l</sup>	56872 <sup>m</sup>	3.28	Swift
DES15S2nr	0.220	1099	57251 <sup>n</sup>	57251 <sup>o</sup>	3.02	Swift
SN 2016ard/PS16aqv	0.2025 <sup>p</sup>	988	57438 <sup>q</sup>	57393 <sup>r</sup>	3.97	Swift

<sup>a</sup>From [Levan et al. 2013](#).<sup>b</sup>From [Quimby et al. \(2011c\)](#), the peak time is MJD 55069.145 and the rest-frame rise-time is  $\sim 50$  days.<sup>c</sup>From [Quimby et al. \(2011c\)](#), the peak time is MJD 55279 and the rest-frame rise-time is  $\sim 23$  days.<sup>d</sup>[Vinko et al. \(2012\)](#) report that SN2010kd reached maximum light 40 days after discovery. We assume a 50 day rest-frame rise-time.<sup>e</sup>From [Inserra et al. \(2013\)](#).<sup>f</sup>From [Yan et al. \(2015\)](#).<sup>g</sup>[Yan et al. \(2015\)](#) report a range of explosion dates between MJD 56470.8 and MJD 56522.0. We use the middle date MJD 56496.4.<sup>h</sup>From [Leloudas et al. \(2015a\)](#).<sup>i</sup>Peak time on MJD 56699 ([Leloudas et al. 2015a](#)). The pre-max evolution is only sparsely sampled (see [Leloudas et al. 2015a](#)). We assume a 50-day rest-frame rise-time, similar to other SLSNe-I.<sup>j</sup>From [Jerkstrand et al. \(2016\)](#).<sup>k</sup>From the CRTS source catalog <http://nesssi.cacr.caltech.edu/catalina/ALLSN.html><sup>l</sup>From [Smith et al. \(2014\)](#).<sup>m</sup>According to [Smith et al. \(2014\)](#), on Nov 22, 2014 the transient was 4-5 weeks rest-frame after maximum light. The inferred time of maximum light is MJD 56940. We assume a 50-day rest-frame rise-time.<sup>n</sup>From [D'Andrea et al. \(2015\)](#).<sup>o</sup>Very sparse photometric coverage. On MJD 57286 [D'Andrea et al. \(2015\)](#) report that the transient is still before peak. We adopt the discovery date as a rough proxy for the explosion date here.<sup>p</sup>From [Blanchard et al.](#), in prep.<sup>q</sup>From <http://star.pst.qub.ac.uk/ps1threepi/psdb/public/><sup>r</sup>The peak time is MJD 57453 from <http://star.pst.qub.ac.uk/ps1threepi/psdb/public/>. We assume a 50-day rest-frame rise time.

ing calibration files. Standard ACIS data filtering has been applied. XMM data have been analyzed with SAS (v15.0). For the non-detections, we perform a flux calibration adopting a power-law spectral model with index  $\Gamma = 2$  corrected for the Galactic neutral-hydrogen absorption along the line of sight (Tables 1, 2, 3), as inferred from [Kalberla et al. \(2005\)](#). The details on X-ray observations of specific SLSNe-I are provided in Sec. 2.1 for the gold sample, and in Appendix A for all the other SLSNe-I. Data tables can also be found in Appendix A. Figure 1 shows the complete sample of X-ray

observations of SLSNe-I.

## 2.1. Gold Sample

There are four objects in the gold sample: SCP06F6, PTF12dam, PS1-14bj, and SN 2015bn (Table 1). In this section we describe the discovery and properties of each object in the gold sample.

### 2.1.1. SCP06F6

TABLE 3  
IRON SAMPLE.

SN	z	$d_L$ (Mpc)	Discovery Date (MJD)	Inferred Explosion Date (MJD)	$N_{H,MW}$ ( $10^{20} \text{ cm}^{-2}$ )	Instrument
SN2009jh/PTF09cwl	0.349	1868	55010 <sup>a</sup>	55010 <sup>b</sup>	1.49	Swift
PTF09atu	0.501	2870	55016 <sup>a</sup>	54988 <sup>c</sup>	3.79	Swift
PTF10aagc	0.207	1027	Unclear	55413 <sup>d</sup>	2.61	Swift
SN 2010md/PTF10hgi	0.098	463	55331 <sup>a</sup>	55323 <sup>e</sup>	5.81	Swift
PS1-11bdn	0.738	4601	55910.4 <sup>f</sup>	55889.2 <sup>f</sup>	3.76	Swift
PTF11rks	0.19	933	55916 <sup>a</sup>	55912 <sup>e</sup>	4.66	Swift
DES15C3hav	0.392	2142	57310 <sup>g</sup>	57270 <sup>h</sup>	0.705	Swift
OGLE15qz	0.63	3790	57264	57264 <sup>i</sup>	4.28	Swift
OGLE15sd	0.656	3319	57295	57295 <sup>i</sup>	9.44	Swift
PS16op	0.48	2726	57398 <sup>j</sup>	57323 <sup>k</sup>	6.73	Swift

<sup>a</sup>From [Levan et al. \(2013\)](#).<sup>b</sup>The time of peak is MJD 55081 and the rise time is  $\sim 50$  days in the rest frame ([Quimby et al. 2011c](#)).<sup>c</sup>The time of maximum light is MJD 55063 ([Quimby et al. 2011c](#)). We assume a 50-day rise-time in the rest-frame.<sup>d</sup>The time of maximum light is MJD 55473 ([Perley et al. 2016](#)). We assume a 50 day rise-time in the rest frame.<sup>e</sup>From [Inserra et al. \(2013\)](#).<sup>f</sup>From Lunnan et al., in prep.<sup>g</sup>From [Challis et al. \(2016\)](#).<sup>h</sup>From [Challis et al. \(2016\)](#) the peak time is MJD 57340. We assume a 50 day rest-frame rise-time.<sup>i</sup>From <http://ogle.astrouw.edu.pl/ogle4/transients/transients.html><sup>j</sup>From [Dimitriadis et al. \(2016\)](#).<sup>k</sup>The peak time is MJD 57397 ([Dimitriadis et al. 2016](#)). We assume a 50 day rest-frame rise-time.TABLE 4  
MAGNETAR PARAMETERS (MAGNETIC FIELD  $B$ , SPIN PERIOD  $P_i$  AND EJECTA MASS  $M_{ej}$ ), ESTIMATED FROM THE BOLOMETRIC OPTICAL EMISSION, AND CORRESPONDING IONIZATION BREAK OUT TIMES  $t_{ion}$  AND X-RAY LUMINOSITIES  $L_x(t_{ion})$ 

SN	$B$ (G)	$P_i$ (ms)	$M_{ej}$ ( $M_\odot$ )	Ref	$t_{ion}$ (yr)	$L_x(t_{ion})$ ( $\text{erg s}^{-1}$ )
SN 2010md/PTF10hgi	$3.6 \times 10^{14}$	7.2	3.9	<a href="#">Inserra et al. (2013)</a>	76.3	$7.8 \times 10^{36}$
SN 2010gx	$7.4 \times 10^{14}$	2.0	7.1	<a href="#">Inserra et al. (2013)</a>	1070	$9.4 \times 10^{33}$
PTF11rks	$6.8 \times 10^{14}$	7.50	2.8	<a href="#">Inserra et al. (2013)</a>	140	$6.5 \times 10^{35}$
SN 2011ke	$6.4 \times 10^{14}$	1.7	8.6	<a href="#">Inserra et al. (2013)</a>	1170	$1.0 \times 10^{34}$
PTF12dam	$5 \times 10^{13}$	2.3	7	<a href="#">Nicholl et al. (2013)</a>	4.7	$1.0 \times 10^{41}$
SN 2012il	$4.1 \times 10^{14}$	6.1	2.3	<a href="#">Inserra et al. (2013)</a>	34.5	$3.0 \times 10^{37}$
iPTF13ehe	$8 \times 10^{13}$	2.55	35	<a href="#">Wang et al. (2015)</a>	304	$1.0 \times 10^{37}$
PS1-14bj	$10^{14}$	3.1	22.5	<a href="#">Lunnan et al. (2016)</a>	196	$1.5 \times 10^{37}$
	$5 \times 10^{13}$	3.1	16	<a href="#">Lunnan et al. (2016)</a> w. leakage	24.8	$3.8 \times 10^{39}$
SN 2015bn/PS15ae	$0.9 \times 10^{14}$	2.1	8.4	<a href="#">Nicholl et al. (2016a)</a>	22.1	$1.5 \times 10^{39}$
	$10^{14}$	1.7	15.1	<a href="#">Nicholl et al. (2016a)</a>	88.4	$7.6 \times 10^{37}$
	$0.9 \times 10^{14}$	2.1	8.3	<a href="#">Nicholl et al. (2016b)</a>	21.6	$1.6 \times 10^{39}$
	$0.2 \times 10^{14}$	1.5	7.4	<a href="#">Nicholl et al. (2016b)</a>	0.64	$3.5 \times 10^{43}$
	$0.9 \times 10^{14}$	2.2	11.9	<a href="#">Nicholl et al. (2016b)</a>	44.5	$3.7 \times 10^{38}$
	$0.4 \times 10^{14}$	1.8	9.0	<a href="#">Nicholl et al. (2016b)</a>	5.02	$1.5 \times 10^{41}$

X-ray emission at the location of the type-I SLSN SCP06F6 was first reported by [Gänsicke et al. \(2009\)](#) from XMM observations obtained 162 days after the initial detection of SCP06F6 (PI Shartel, ID 0410580301). [Levan et al. \(2013\)](#) derive an X-ray flux  $F_x \sim 10^{-13} \text{ erg s}^{-1} \text{ cm}^{-2}$  (0.3–10 keV) on 2006 August 2 (MJD 53949,  $\sim 80$  days rest-frame since explosion). Follow-up observations with the CXO obtained on 2006 November 4 (MJD 54043,  $\sim 126$  days rest-frame since explosion, PI Murray, ID 7010) led to a non-detection. The corresponding flux limit is  $F_x < 1.4 \times 10^{-14} \text{ erg s}^{-1} \text{ cm}^{-2}$  ([Levan et al. 2013](#)). We adopt these values here and refer to [Levan et al. \(2013\)](#) for further details. We note there that the correct redshift for this event is  $z = 1.189$  ([Quimby et al. 2011c](#)).

#### 2.1.2. X-ray emission at the location of PTF12dam

PTF12dam ([Nicholl et al. 2013](#); [Chen et al. 2015](#); [Inserra et al. 2017](#); [Vreeswijk et al. 2017](#)) belongs to the small subset of SLSNe-I with slowly evolving optical light-curves. At the time of writing, this group includes SN 2007bi, PTF12dam, iPTF13ehe, SN2015bn, PS1-14bj and LSQ14an. The slow evolution of these transients, and of SN 2007bi in particular, inspired a connection with pair instability explosions ([Gal-Yam et al. 2009](#)) that was later debated by [Nicholl et al. \(2013\)](#). X-ray observations of the SLSN-I PTF12dam have been obtained with *Swift*-XRT and the CXO. *Swift*-XRT observations span the time range  $\sim 43$ –900 days rest-frame since explosion and revealed no detection down to a flux limit  $F_x \sim 5 \times 10^{-14} \text{ erg s}^{-1} \text{ cm}^{-2}$  (Fig. 2, Table 5).



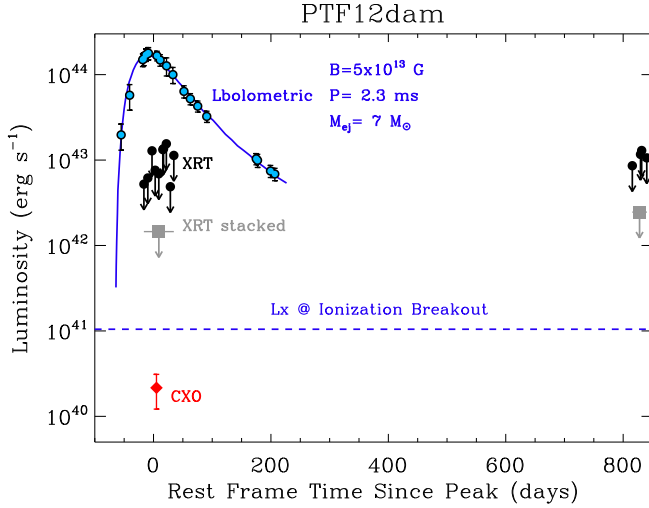


FIG. 2.— Deep CXO observations (red diamond) obtained around the time of optical peak reveal the presence of soft X-ray emission at the location of PTF12dam with luminosity  $L_x \sim 2 \times 10^{40} \text{ erg s}^{-1}$ . Black filled circles: X-ray luminosity limits from *Swift*-XRT. Grey filled squares: stacked limits from *Swift*-XRT observations. Blue filled circles: bolometric optical emission as computed by Nicholl et al. (2013). Blue solid line: best-fitting magnetar model from Nicholl et al. (2013) with parameters reported in Table 4. Horizontal blue dashed line: X-ray luminosity at the time of ionization breakout according to the equations in Sec. 5.2 for the best fitting magnetar parameters (Table 4). The expected time of ionization breakout is  $t_{\text{ion}} = 4.7 \text{ yr}$ , see Table 4.

A set of three deep CXO observations have been acquired between 2012 June 11 and June 19 ( $\delta t \sim 60\text{--}68$  days rest-frame since explosion; observations IDs 13772, 14444 and 14446, PI Pooley). An X-ray source with a soft spectrum is clearly detected in the merged event file (total exposure of 99.9 ks) at the location of PTF12dam with significance of  $4.8\sigma$  in the 0.5-2 keV energy range. The measured net count-rate is  $(7.1 \pm 2.8) \times 10^{-5} \text{ cs}^{-1}$  (0.5-2 keV), which corresponds to an unabsorbed flux of  $(7.3 \pm 2.9) \times 10^{-16} \text{ erg s}^{-1} \text{ cm}^{-2}$  (0.3-10 keV) assuming a power-law spectrum with photon index  $\Gamma = 2$ . For a thermal bremsstrahlung spectrum with  $T = 0.24 \text{ keV}$  (see below) the corresponding unabsorbed flux is  $(8.9 \pm 3.5) \times 10^{-16} \text{ erg s}^{-1} \text{ cm}^{-2}$  (0.3-10 keV), and  $(3.5 \pm 1.4) \times 10^{-16} \text{ erg s}^{-1} \text{ cm}^{-2}$  (0.5-2 keV). In both cases, the inferred X-ray luminosity is  $L_x \sim 2 \times 10^{40} \text{ erg s}^{-1}$  in the 0.3-10 keV (Fig. 2).

PTF12dam exploded in a compact dwarf galaxy with fairly large star formation rate  $SFR \sim 5 M_{\odot} \text{ yr}^{-1}$  (Lunnan et al. 2014; Chen et al. 2015; Thöne et al. 2015; Leloudas et al. 2015b; Perley et al. 2016)<sup>12</sup>. Following Mineo et al. (2012), the expected apparent diffuse X-ray emission associated with star formation is  $L_x/SFR \approx 8.3 \times 10^{38} \text{ erg s}^{-1} (M_{\odot} \text{ yr}^{-1})^{-1}$ , which translates into  $L_x \approx 4.2 \times 10^{39} \text{ erg s}^{-1}$  (0.5-2 keV) for  $SFR \sim 5 M_{\odot} \text{ yr}^{-1}$ . As a comparison, for a thermal bremsstrahlung spectrum with  $T = 0.24 \text{ keV}$  (average temperature of the unresolved X-ray component in galaxies, Mineo et al. 2012), for PTF12dam we calculate  $L_x \approx (1.0 \pm 0.4) \times 10^{40} \text{ erg s}^{-1}$  (0.5-2 keV). We therefore conclude that star formation in the host galaxy of PTF12dam is likely contributing to at least some of the X-ray luminosity that we detected at the location of the transient. In the following analysis sections we

<sup>12</sup> While Lunnan et al. (2014), Chen et al. (2015), Thöne et al. (2015) and Leloudas et al. (2015b) measure  $SFR \sim 5 M_{\odot} \text{ yr}^{-1}$ , Perley et al. (2016) report an even larger  $SFR \sim 10 M_{\odot} \text{ yr}^{-1}$ .

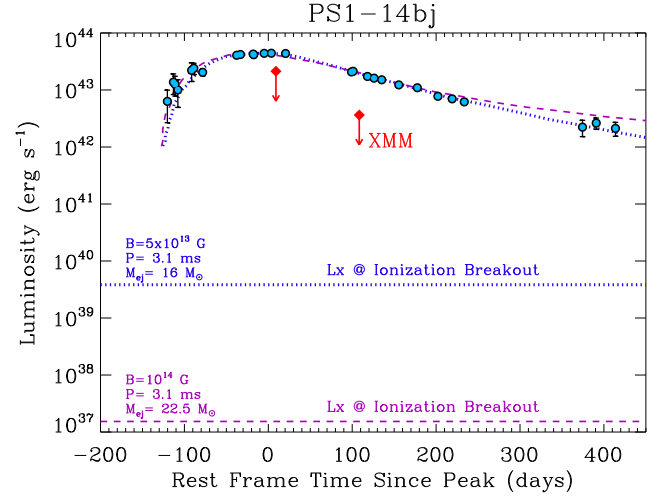


FIG. 3.— Luminosity limits on the X-ray emission from PS1-14bj obtained with XMM (red diamonds). Blue filled circles: bolometric luminosity as computed by Lunnan et al. (2016). Blue dotted line and purple dashed line: magnetar models that adequately fit the observations as computed by Lunnan et al. (2016) (see Table 4). Horizontal lines: X-ray luminosity at the time of ionization breakout according to the equations in Sec. 5.2 for the two magnetar models. For these models, the expected time of ionization breakout is  $t_{\text{ion}} \geq 25 \text{ yr}$ , see Table 4.

treat our measurements as upper limits to the X-ray emission from PTF12dam. These observations provide the deepest limits to the X-ray emission from a SLSN-I to date. Future observations will constrain the late-time behavior of the X-ray emission at the location of PTF12dam and will clarify its association to the optical transient.

### 2.1.3. PS1-14bj

Two epochs of deep X-ray observations of the type-I SLSN PS1-14bj (Lunnan et al. 2016) have been obtained with XMM (PI Margutti, IDs 0743110301, 0743110701) on 2014 June 9 ( $\delta t \sim 135$  days rest-frame since explosion, exposure time of 47.6 ks), and 2014 Nov 7 ( $\delta t \sim 235$  days rest-frame since explosion, exposure of 36.0 ks). The net exposure times after removing data with high background contamination are 3.6 ks and 29.8 ks, respectively (EPIC-pn data). We do not find evidence for significant X-ray emission at the location of PS1-14bj in either observation and derive a  $3\sigma$  0.3-10 keV count-rate upper limit of  $9.4 \times 10^{-3} \text{ cs}^{-1}$  ( $1.5 \times 10^{-3} \text{ cs}^{-1}$ ) for the first (second) epoch, which translates into an unabsorbed flux of  $1.9 \times 10^{-14} \text{ erg s}^{-1} \text{ cm}^{-2}$  ( $3.3 \times 10^{-15} \text{ erg s}^{-1} \text{ cm}^{-2}$ ). The corresponding luminosity limits are shown in Fig. 3 and reported in Table 5.

### 2.1.4. SN2015bn

X-ray observations of the SLSN-I 2015bn (Nicholl et al. 2016a,b) have been obtained with *Swift*-XRT and XMM (PI Margutti, IDs 0770380201, 0770380401). A first set of observations have been presented in Nicholl et al. (2016b), while Inserra et al. (2017) include in their analysis five *Swift*-XRT pointings. Here we present the complete data set. *Swift*-XRT started observing SN2015bn on 2015 February 19 until 2016 July 23 covering the time period  $\sim 44\text{--}522$  days since explosion rest-frame. No statistically significant X-ray emission is blindly detected at the location of the transient (Fig. 4).<sup>13</sup>

<sup>13</sup> We note the presence of marginally significant ( $2\sigma$  c.l.) soft X-ray emission (i.e.  $< 0.3 \text{ keV}$ ) with  $L_x \sim 5 \times 10^{42} \text{ erg s}^{-1}$  found in a targeted search of

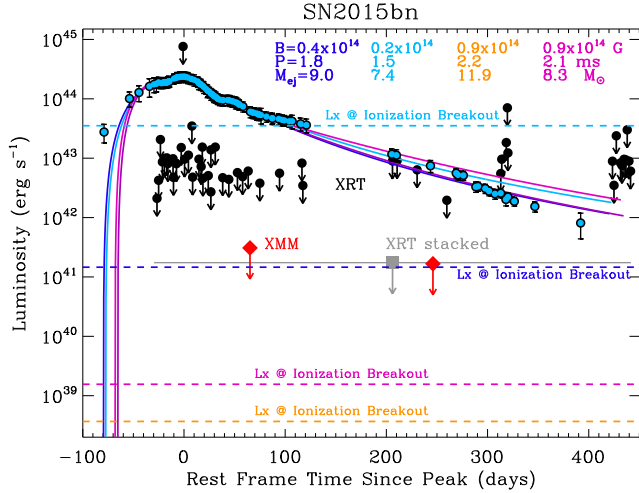


FIG. 4.— Results from our joint *Swift*-XRT and XMM X-ray campaign (black filled circles, grey squares and red diamonds) in the context of the optical bolometric luminosity of SN2015bn and the best-fitting magnetar models as derived by Nicholl et al. (2016a) (see Table 4). Horizontal dashed lines: expected X-ray luminosity at the time of the ionization breakout, which is  $t_{\text{ion}} = 5$  yrs (for  $B = 0.4 \times 10^{14}$  G,  $P = 1.8$  ms,  $M_{\text{ej}} = 9 M_{\odot}$ ),  $t_{\text{ion}} = 0.6$  yr (for  $B = 0.2 \times 10^{14}$  G,  $P = 1.5$  ms,  $M_{\text{ej}} = 7.4 M_{\odot}$ ),  $t_{\text{ion}} = 45$  yr (for  $B = 0.9 \times 10^{14}$  G,  $P = 2.2$  ms,  $M_{\text{ej}} = 11.9 M_{\odot}$ ),  $t_{\text{ion}} = 22$  yr (for  $B = 0.9 \times 10^{14}$  G,  $P = 2.1$  ms,  $M_{\text{ej}} = 8.3 M_{\odot}$ ) as reported in Table 4. The models with the shortest spin periods are disfavored by our X-ray limits. This figure clearly shows how magnetar models associated with very similar bolometric optical light-curves do predict instead very different X-ray luminosities at ionization breakout. The X-ray luminosity at the time of breakout is a very sensitive probe of the properties of central engines in SLSNe.

Two epochs of XMM observations have been obtained on 2015 June 1 ( $\delta t \sim 145$  days rest frame since explosion) and 2015 Dec 18 ( $\delta t \sim 325$  days rest frame since explosion) with exposure times of 28.0 ks and 25.1 ks, respectively (EPIC-pn data). After excluding time intervals heavily affected by proton flaring, the net exposure times are 7.3 ks and 18.8 ks. No X-ray source is detected at the location of the SLSN-I 2015bn. We derive a  $3\sigma$  0.3-10 keV count-rate upper limit of  $4.2 \times 10^{-3} \text{ cs}^{-1}$  ( $2.3 \times 10^{-3} \text{ cs}^{-1}$ ) for the first (second) epoch, which translates into an unabsorbed flux of  $9.8 \times 10^{-15} \text{ erg s cm}^{-2}$  ( $5.3 \times 10^{-15} \text{ erg s cm}^{-2}$ ). The results from our X-ray campaign are listed in Table 5 and displayed in Fig. 4.

### 3. SEARCH FOR SUPERLUMINOUS X-RAY EMISSION IN SLSNE-I

In this section we derive constraints on the possible presence of superluminous X-ray emission in SLSNe-I that was not detected because of the discontinuous observational coverage. No assumption is made about the physical nature of the emission. SLSNe-I are treated here as different realizations of the same stochastic process (which is the underlying assumption behind any sample analysis).

The hypothesis we test is that superluminous X-ray emission of the kind detected at the location of SCP06F6 (i.e.

data acquired on 2015 Feb 22 (i.e.  $\sim 55$  days since explosion, rest frame). However, emission with this flux is ruled out by *Swift*-XRT observations obtained 24 hrs before, and is not detected in *Swift*-XRT data with similar exposure time collected in the days afterwards. Furthermore, we find no evidence for X-ray emission when we filter the event file in the standard 0.3-10 keV energy range, which is where the *Swift*-XRT is properly calibrated. We conclude that the association of the targeted detection with real X-ray emission from SLSN-I 2015bn/PS15ae is highly questionable and therefore proceed with the conclusion of no statistically significant X-ray emission at the location of the transient.

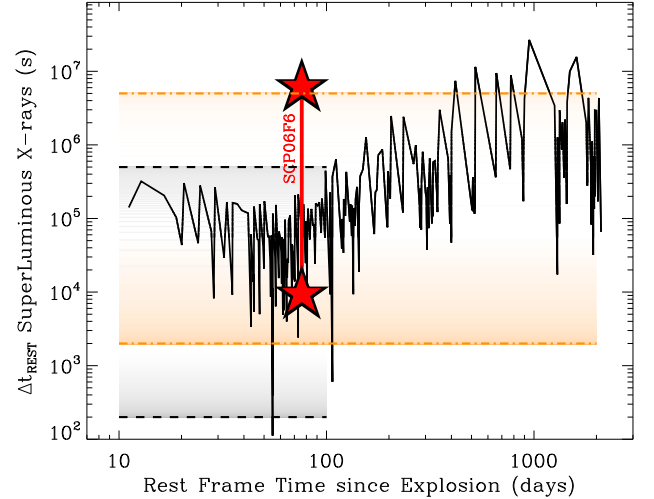


FIG. 5.— Constraints on the duration of undetected superluminous X-ray emission with  $L_x \sim 10^{45} \text{ erg s}^{-1}$  in SLSNe-I. Black line: upper limit to the duration  $\Delta t_{\text{REST}}$  of the (undetected) superluminous X-ray emission from the analysis of the entire sample of SLSNe-I as a function of time since explosion. For SCP06F6, the range of allowed durations is between  $\Delta t_{\text{REST}} \sim 10^4$  s (exposure time of the XMM observation that provided a detection of X-ray emission) and the time of first detection  $\Delta t_{\text{REST}} \sim 70$  days (red stars). Horizontal black dashed lines: range of  $3\sigma$  c.l. allowed  $\Delta t_{\text{REST}}$  based on the statistical analysis of observations of SLSNe-I in the first 100 days since explosion. Orange dot-dashed lines:  $3\sigma$  c.l. for  $t < 2000$  days since explosion.

$L_x \sim 10^{45} \text{ erg s}^{-1}$ ) is ubiquitous in SLSNe-I. Our sample of observations comprises 253 spacecraft pointings, for a total observing time of  $\sim 30$  days at  $t < 2000$  days (rest frame). Out of 253 trials, observations only led to one success (i.e. in the case of SCP06F6). By using simple binomial probability arguments, we constrain the maximum and minimum  $\Delta t_{\text{REST}}$  that would be statistically consistent at the  $3\sigma$  c.l. with 1 success out of  $N$  trials, where  $N \equiv N(t)$  and  $N = 253$  for  $t = 2000$  days. For  $t < 100$  days we find  $200 \text{ s} \leq \Delta t_{\text{REST}} \leq 5 \times 10^5 \text{ s}$ , while for  $t < 2000$  days we find  $2000 \text{ s} \leq \Delta t_{\text{REST}} \leq 5 \times 10^6 \text{ s}$  (Fig. 5, horizontal lines). In Figure 5, we also show with a thick black line the maximum duration of the superluminous X-ray emission that would be consistent with the lack of detections in our sample of SLSNe-I as a function of time since explosion.

We conclude that superluminous X-ray emission is not a common trait of SLSNe-I. If present, the superluminous X-ray emission requires peculiar physical circumstances to manifest and its duration is  $\leq 2$  months at  $t < 2000$  days and  $\leq$  few days at  $t < 100$  days.

### 4. CONSTRAINTS ON SLSNE-I ENVIRONMENTS

Inverse Compton (IC) emission is a well known source of X-rays in young stellar explosions (Björnsson & Fransson 2004; Chevalier & Fransson 2006). X-ray emission originates from the up-scattering of optical photons from the SN photosphere by a population of relativistic electrons accelerated at the shock front. While always present, IC is the dominant emission mechanism at early times ( $t \leq$  optical peak) for SN propagating into low-density media. In the case of strong SN shock interaction with the medium, the dominant X-ray emission mechanism is instead bremsstrahlung (Björnsson & Fransson 2004; Chevalier & Fransson 2006) as it is indeed observed in type-IIIn SNe and as recently confirmed by the first broad-band X-ray spectra of strongly interacting SNe (Ofek et al. 2014; Margutti et al. 2017a). The analysis of the optical emission from SLSNe-I in the context of the interaction model

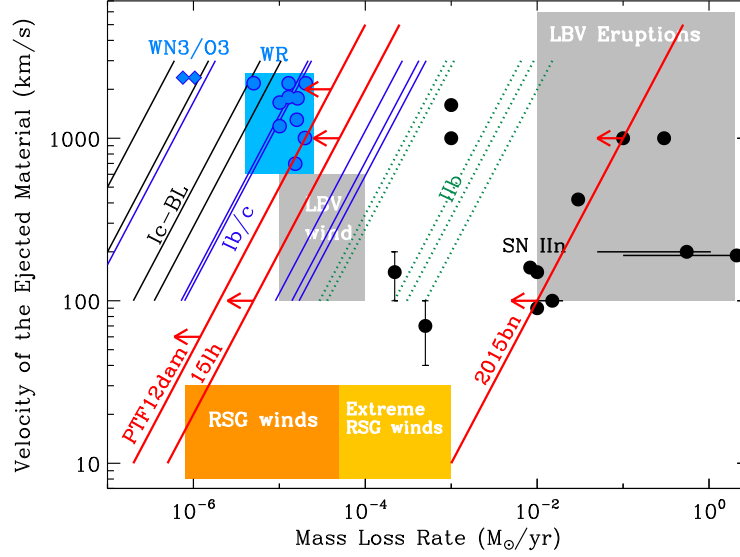


FIG. 6.— Velocity of the ejected material during mass loss vs. pre-explosion mass-loss rate for H-poor core-collapse SNe (diagonal lines) and type-II SNe (black dots). H-poor SNe are represented with diagonal lines since radio and X-ray observations constrain the density  $\rho_{CSM}$  which is  $\propto \dot{M}/v_w$ . Black, blue and dotted green lines mark the sample of type Ic-BL, Ib/c and IIb SNe from Drout et al. 2016. SLSNe-I and the transient ASASSN-15lh are in red. For SLSNe-I we conservatively plot the constraints for  $E_k = 10^{51}$  erg, which is a lower limit to the total kinetic energy of the blastwave (even in the case of a magnetar central engine). The properties of galactic WR stars are from Crowther (2007), while WN3/O3 stars are from Massey et al. (2015). Locations of red supergiants environments (RSG) are from de Jager et al. (1988), Marshall et al. (2004) and van Loon et al. (2005). Typical locations of Luminous Blue Variable (LBV) winds and eruptions are from Smith (2014) and Smith & Owocki (2006). The densest environments that characterize LBV eruptions and type-II SNe are not consistent with our deepest SLSNe-I limits. Our tightest constraints on PTF12dam rule out RSG winds and put PTF12dam in the same region of the parameter space as H-stripped SNe with broad spectral features (i.e. Ic-BL).

(e.g. Nicholl et al. 2014, 2016a) suggests that *if* SLSNe-I are powered by interaction then the shock breaks out around the time of optical maximum light and the medium consists of a thick shell confined to small radii ( $R \sim 5 \times 10^{15}$  cm for SN2015bn) surrounded by a lower density region. This conclusion is consistent with the lack of observed narrow lines in the optical spectra of SLSNe-I (in sharp contrast to ordinary and superluminous type-II SNe): the presence of an extended unshocked region of dense CSM would likely imprint low-velocity features which are *not* observed in SLSNe-I (see also Chevalier & Irwin 2011). The X-ray observations that we will use in this section have been obtained at the time of maximum light or later, which is after the shock has broken out from the thick shell of material *if* a shell is there. In the following, we thus constrain the density around SLSNe-I under the conservative assumption that IC is the *only* source of X-ray radiation. Since we sample the time range  $t > t_{peak}$ , our density limits apply to the region  $R \gtrsim 10^{16}$  cm.

The X-ray emission from IC depends on (i) the density structure of the SN ejecta and of the circum-stellar medium (CSM), (ii) the details of the electron distribution responsible for the up-scattering, (iii) the explosion parameters (ejecta mass  $M_{ej}$  and kinetic energy  $E_k$ ), and (iv) the availability of seed optical photons ( $L_{x,IC} \propto L_{bol}$ , where  $L_{bol}$  is the bolometric optical luminosity). We employ the formalism of Margutti et al. (2012) modified to reflect the stellar structure of massive stars as in Margutti et al. (2014). We further assume a wind-like medium with  $\rho_{CSM} \propto R^{-2}$  as appropriate for massive stars, a power-law electron distribution  $n_e(\gamma) = n_0 \gamma^{-p}$  with  $p \sim 3$  as indicated by radio observations of H-stripped core-collapse SNe (Chevalier & Fransson 2006) and a fraction of post-shock energy into relativistic electrons  $\epsilon_e = 0.1$  (e.g. Chevalier & Fransson 2006). Since  $L_{x,IC} \propto L_{bol}$ , it is clear that the tightest constraints on  $\rho_{CSM}$  will be derived from the most nearby SLSNe-I, which have very bright optical emission and deep

X-ray limits (i.e. they have the largest flux ratio  $F_{opt}/F_x$  constrained by observations). To this end, we analyze below the SLSNe-I 2015bn and PTF12dam. We also provide constraints for the peculiar transient ASASSN-15lh.

For SN2015bn we follow Nicholl et al. (2016b) and Nicholl et al. (2016a) and adopt a range of ejecta masses  $M_{ej} = 7 - 15 M_\odot$  (Table 4). With these parameters and the optical bolometric light-curve from Nicholl et al. (2016a) (Fig. 4), our X-ray non detections constrain the pre-explosion mass-loss rate from the stellar progenitor of SN2015bn to  $\dot{M} < 10^{-2} M_\odot \text{yr}^{-1}$  ( $\dot{M} < 10^{-1} M_\odot \text{yr}^{-1}$ ) for  $E_k = 10^{52}$  erg ( $E_k = 10^{51}$  erg) and wind velocity  $v_w = 1000 \text{ km s}^{-1}$ , (Fig. 6, 7), which is  $\dot{M} < 10^{-4} M_\odot \text{yr}^{-1}$  ( $\dot{M} < 10^{-3} M_\odot \text{yr}^{-1}$ ) for wind velocity  $v_w = 10 \text{ km s}^{-1}$ . In this context, the analysis of the radio observations of SN2015bn indicates  $\dot{M} < 10^{-2} M_\odot \text{yr}^{-1}$  for  $v_w = 10 \text{ km s}^{-1}$  at  $R > 10^{15}$  cm, while  $\dot{M} \sim 10^{-2} M_\odot \text{yr}^{-1}$  would be needed to explain the late-time optical light curve of the transient through continued ejecta-CSM interaction (Nicholl et al. 2016a). The X-ray analysis thus argues against the presence of an extended CSM region if  $E_k > 10^{51}$  erg (as it is likely the case) and suggests that another source of energy is powering the light-curve after peak. This result is consistent with the conclusions by Nicholl et al. (2016b): based on the spectroscopic similarity of SN2015bn with the GRB SN1998bw in the nebular phase, Nicholl et al. (2016b) concluded that a central engine is driving the explosion.

For PTF12dam we use  $M_{ej} = 7 M_\odot$  as inferred by Nicholl et al. (2013) from the modeling of the optical bolometric emission (Table 4). We detect an X-ray source at the location of PTF12dam with  $L_x \sim 2 \times 10^{40} \text{ erg s}^{-1}$ . We treat this value as an upper limit to the X-ray luminosity from the transient to account for possible contamination from the host galaxy. For these values of the explosion parameters and the measured  $L_x$ , the inferred mass-loss rate is  $\dot{M} < 2 \times 10^{-5} M_\odot \text{yr}^{-1}$



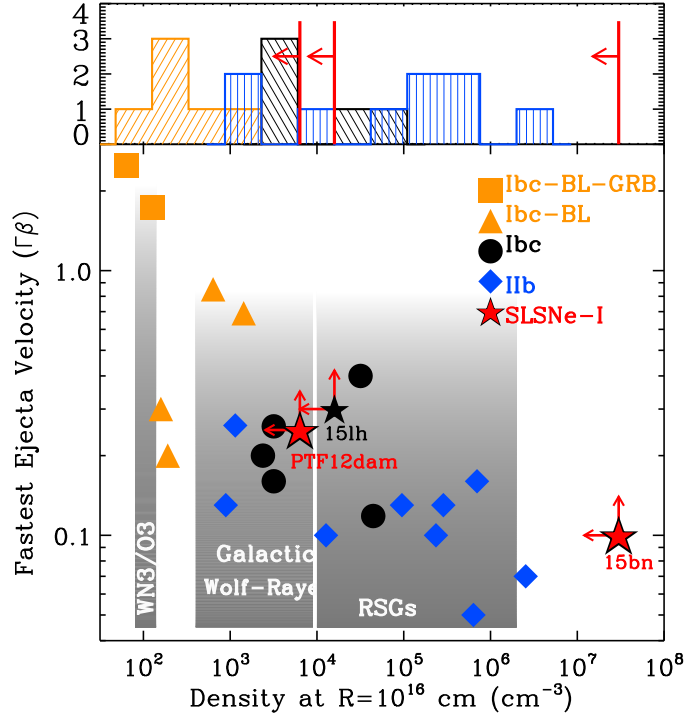


FIG. 7.— Constraints on the fastest SN ejecta velocity and environmental density of SLSNe-I with the most sensitive X-ray limits (red stars) and the peculiar transient ASASSN-15lh (black star) in the context of core-collapse stellar explosions from H-stripped progenitors. Grey shaded regions: density in the environments of Red Supergiant Stars (RSGs), Wolf-Rayet stars (WRs) and the recently discovered new type of WR stars WN3/O3 (de Jager et al. 1988; Marshall et al. 2004; van Loon et al. 2005; Crowther 2007; Massey et al. 2015). Type IIb SNe (blue diamonds) explode in the densest environments, while SNe with broad spectroscopic features (orange squares and triangle) are associated with the lowest density media. For SLSNe-I we conservatively plot the constraints for  $E_k = 10^{51}$  erg, which is a *lower limit* to the total kinetic energy of the blastwave (even in the case of a magnetar central engine). In the case of PTF12dam, our measurements rule out the dense environments associated with RSG winds and are consistent with the clean environments that characterize WRs, WN3/O3 and engine-driven SN explosions. References: van Dyk et al. (1994); Fransson & Björnsson (1998); Berger et al. (2002); Weiler et al. (2002); Ryder et al. (2004); Soderberg et al. (2005); Chevalier & Fransson (2006); Soderberg et al. (2006a,b, 2008); Roming et al. (2009); Soderberg et al. (2010b,a); Krauss et al. (2012); Milisavljevic et al. (2013); Margutti et al. (2014); Kamble et al. (2014); Corsi et al. (2014); Chakraborti et al. (2015); Drout et al. (2016); Kamble et al. (2016); Margutti et al. (2017a).

( $\dot{M} < 4 \times 10^{-6} M_{\odot} \text{yr}^{-1}$ ) for  $E_k = 10^{51}$  erg ( $E_k = 10^{52}$  erg) and  $v_w = 1000 \text{ km s}^{-1}$  (Fig. 6, 7). These are the tightest constraints to the pre-explosion mass-loss history of SLSNe-I progenitors.

If the peculiar transient ASASSN-15lh is associated with an  $E_k = 10^{52}$  erg explosion with ejecta mass  $M_{ej} = 5 - 10 M_{\odot}$  (Metzger et al. 2015; Chatzopoulos et al. 2016; Dong et al. 2016; Kozyreva et al. 2016; Sukhbold & Woosley 2016; Bersten et al. 2016; Dai et al. 2016), the X-ray observations from Margutti et al. (2017b), imply  $\dot{M} < 5 \times 10^{-6} M_{\odot} \text{yr}^{-1}$  ( $\dot{M} < 5 \times 10^{-5} M_{\odot} \text{yr}^{-1}$ ) for  $v_w = 1000 \text{ km s}^{-1}$  for a thermal (non thermal) X-ray spectrum. These values are typical of mass-loss rates from H-stripped compact massive stars (Fig. 6, 7).

We end by noting that the calculations of the expected X-ray luminosity from the strong interaction scenario applied to SLSNe-I reported in Inserra et al. (2017) provide *upper limits* to the X-ray luminosity from the interaction scenario rather than expected  $L_x$  as it is assumed that as much as 10% of the total kinetic energy is converted into X-ray photons in the 0.3-10 keV energy range that would leak out and reach the observer without being absorbed, thermalized and/or downgraded to lower energies due to scattering processes within the dense media. For this reason, the large  $L_x \sim 10^{43} \text{ erg/s}$  predicted with this method by Inserra et al. (2017) cannot be directly compared to the observed X-ray limits and cannot be used to rule out the strong interaction scenario. As a matter of

fact, the SLSN-II in 2006gy is maybe the most extreme example of SLSN powered by interaction with a massive CSM shell with  $M \sim 10 M_{\odot}$  and it was detected in the X-rays around optical maximum light with  $L_x \sim 10^{39} \text{ erg/s}$  which is clearly  $\ll 10^{43} \text{ erg/s}$  (Smith et al. 2007).

From our analysis, we conclude that for PTF12dam the inferred limits rule out the densest environments that characterize type-II In SNe (Fig. 6), indicating that the strong SN shock interaction with an *extended* medium is unlikely to be the primary source of energy sustaining the very luminous display. Interestingly, a low-density environment with  $\dot{M} \sim 4 \times 10^{-6} M_{\odot} \text{yr}^{-1}$  was also inferred from radio and X-ray observations of the type-Ib SN 2012au (Kamble et al. 2014), which showed spectroscopic similarities with SLSN-I (Milisavljevic et al. 2013). The tight constraints obtained for PTF12dam point to a clean environment, and argue against the dense CSM typical of extended progenitors like RSG stars. This result suggests that at least some SLSN-I progenitors are likely to be compact stars surrounded by a low density medium at the time of stellar death.

## 5. CENTRAL ENGINES IN SLSNE-I

### 5.1. Constraints on on-axis and off-axis collimated and non-collimated relativistic outflows

The search for off-axis and on-axis relativistic GRB-like jets in SLSNe-I is motivated by two recent observational findings: (i) the association of SN2011kl with GRB111209A.



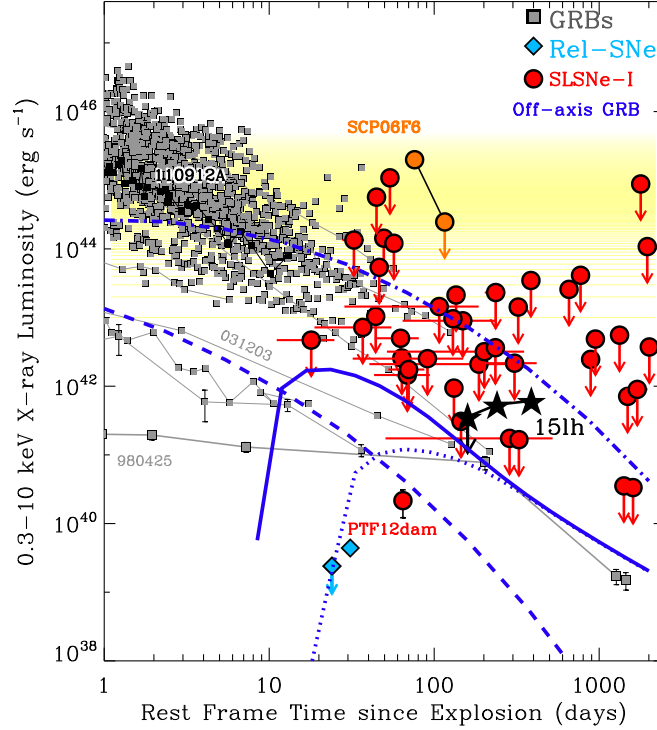


FIG. 8.— X-ray emission from SLSNe-I (red circles) in the context of detected GRB X-ray afterglows (grey squares, Margutti et al. 2013a), relativistic SNe (blue diamonds, Soderberg et al. 2010b; Margutti et al. 2014) and representative off-axis afterglow models (blue lines) from collimated outflows with  $\theta_{\text{jet}} = 5^\circ$ ,  $\epsilon_e = 0.1$ ,  $\epsilon_B = 0.01$ ,  $E_k = 4 \times 10^{52}$  erg,  $\dot{M} = 10^{-3} M_\odot \text{yr}^{-1}$ ,  $\theta_{\text{obs}} = 30^\circ$  (thick line) and  $\theta_{\text{obs}} = 45^\circ$  (dotted line). We also show models for  $\dot{M} = 10^{-7} M_\odot \text{yr}^{-1}$ ,  $\theta_{\text{obs}} = 2\theta_{\text{jet}}$ ,  $E_k = 4 \times 10^{52}$  erg (dot-dashed line) and  $E_k = 4 \times 10^{50}$  erg (dashed line). The fast-fading X-ray emission at the location of SCP06F6 is shown with orange circles (Levan et al. 2013). Black stars: steady X-ray emission at the location of ASASSN-15lh (Margutti et al. 2017b). Black squares: X-ray afterglow of GRB 111209A, associated with the SLSN 2011kl (Greiner et al. 2015). In this plot we show the *Swift*-XRT limits from the stacked analysis for displaying purposes. The analysis and results are based on the time-resolved observations. Notably, our deepest limits rule out non-collimated outflows from the weakest GRB explosions, like GRB 980425 (Pian et al. 2000; Kouveliotou et al. 2004).

SN2011kl bridges the luminosity gap between GRB-SNe and SLSNe-I, and shows spectroscopic similarities to SLSNe-I (Greiner et al. 2015). (ii) Nebular spectroscopy of the SLSN-I 2015bn revealed close similarities to the engine-driven SN1998bw, associated with GRB 980425, suggesting that the core of engine-driven SNe and SLSNe-I share some key physical properties and structure (Nicholl et al. 2016b).

Early-time X-ray observations of SLSNe-I acquired at  $t \lesssim 40$  days generally rule out on-axis collimated ultra-relativistic outflows of the type associated with energetic long GRBs (Fig. 8, cloud of filled grey squares). We constrain the presence of off-axis relativistic outflows by generating a grid of off-axis GRB X-ray afterglows with the broadband afterglow numerical code Boxfit v2 (van Eerten et al. 2012).<sup>14</sup> The observed X-ray emission depends on the kinetic energy  $E_k$  of the outflow, the density of the medium  $\rho_{\text{CSM}}$  (we explore both an ISM-like medium  $n_{\text{CSM}} = \text{const}$  and a wind-like medium with  $\rho_{\text{CSM}} \propto R^{-2}$ ), the microphysical shock parameters  $\epsilon_B$  and  $\epsilon_e$  (postshock energy fraction in magnetic field and electrons, respectively), the jet opening angle  $\theta_j$  and the angle of the jet with respect to the line of sight  $\theta_{\text{obs}}$ . We explore the predicted X-ray signatures of collimated  $\theta_j = 5^\circ$  outflows with  $\epsilon_e = 0.1$  and  $\epsilon_B = 0.01$  (as derived from first-principle simulations of relativistic shocks, e.g. Sironi et al. 2015), isotropic kinetic energy in the range  $E_{k,\text{iso}} = 10^{52} - 10^{55}$  erg, environment density in the range  $n = 10^{-3} - 10 \text{ cm}^{-3}$  (ISM) or mass-loss rate  $\dot{M} = 10^{-7} - 10^{-3} M_\odot \text{yr}^{-1}$  (wind) and observed angles

$\theta_{\text{obs}} \leq 90^\circ$ . These values are representative of the parameters inferred from accurate modeling of broad-band afterglows of GRBs.

Based on these simulations and the X-ray observations from the entire sample of SLSNe-I, we find that relativistic collimated outflows with  $E_k > 10^{51}$  erg,  $n > 10^{-3} \text{ cm}^{-3}$  and  $\theta_{\text{obs}} < 2\theta_j$  are ruled out. Powerful jets with  $E_k > 10^{52}$  erg expanding in a thick medium with  $n \geq 10 \text{ cm}^{-3}$  and  $\theta_{\text{obs}} \leq 30^\circ$  are also ruled out. For a wind environment, our observations are not consistent with jets with  $E_k > 10^{50.5}$  erg expanding in a medium enriched with  $\dot{M} \geq 10^{-7} M_\odot \text{yr}^{-1}$  and  $\theta_{\text{obs}} < 2\theta_j$ . At higher kinetic energies observations rule out jets with  $E_k > 10^{51.5}$  erg,  $\dot{M} \geq 10^{-4} M_\odot \text{yr}^{-1}$  and  $\theta_{\text{obs}} \leq 30^\circ$  or  $E_k > 10^{52}$  erg,  $\dot{M} \geq 10^{-3} M_\odot \text{yr}^{-1}$  and  $\theta_{\text{obs}} \leq 45^\circ$ . We are not sensitive to jets viewed at  $\theta_{\text{obs}} > 30^\circ$  for the ISM, and  $\theta_{\text{obs}} > 45^\circ$  for the wind medium.

In the case of PTF12dam, observations argue against jets with  $E_k > 10^{51}$  erg propagating into a medium with  $n > 10^{-3} \text{ cm}^{-3}$  or  $\dot{M} > 10^{-7} M_\odot \text{yr}^{-1}$  and  $\theta_{\text{obs}} < 2\theta_j$ . The portion of the parameter space associated with  $E_k = 10^{50.5}$  erg,  $\dot{M} \sim 10^{-6-7} M_\odot \text{yr}^{-1}$  and  $\theta_{\text{obs}} < 2\theta_j$  is also ruled out. Dense environments with  $n > 10 \text{ cm}^{-3}$  or  $\dot{M} > 10^{-4} M_\odot \text{yr}^{-1}$  would also produce X-ray emission in excess to what we observed for outflows with  $E_k > 10^{51}$  erg viewed at  $\theta_{\text{obs}} < 30^\circ$ .

For the SLSN-I 2015bn observations rule out systems with  $E_k > 10^{52}$  erg,  $n > 10^{-3} \text{ cm}^{-3}$  or  $\dot{M} > 10^{-7} M_\odot \text{yr}^{-1}$  for  $\theta_{\text{obs}} < 2\theta_j$ . Even the most energetic outflows in our simulations

<sup>14</sup> <http://cosmo.nyu.edu/afterglowlibrary/boxfit2011.html>

with  $E_k > 10^{52}$  erg would fall below our detection threshold for  $\theta_{obs} > 30^\circ$  and the range of densities considered. These observations complement the results from deep radio non-detections of SN2015bn (Nicholl et al. 2016a), which argue against powerful on-axis or off-axis jets with  $E_k = 2 \times 10^{51}$  erg propagating into an ISM-like medium with density  $n = 1 \text{ cm}^{-3}$ .<sup>15</sup>

Finally, we consider the observable X-ray signatures of *non-collimated* mildly-relativistic outflows. X-ray observations of the majority of SLSNe-I in our sample are not sensitive to the faint X-ray emission of mildly-relativistic non-collimated outflows typical of low-energy GRBs like 980425, 031203, 060218 and 100316D (e.g. Pian et al. 2000; Kouveliotou et al. 2004; Watson et al. 2004; Soderberg et al. 2006b; Margutti et al. 2013b). However, our deepest X-ray limits obtained with the CXO and XMM are sensitive enough to probe the parameter space populated by the weakest GRB-SNe. For the SLSN-I 2015bn, our XMM observations probe and rule out luminosities  $L_x > 2 \times 10^{41} \text{ erg s}^{-1}$  at  $t \sim 100$ –300 days, which are comparable to the detected X-ray emission of GRBs 980425 and 031203 at a similar epoch,  $L_x \sim 10^{41} \text{ erg s}^{-1}$  (Fig. 8). Remarkably, in the case of PTF12dam, CXO observations acquired at the time of optical peak rule out even the faintest non-collimated X-ray emission ever detected from a low-energy GRB (Fig. 8), indicating that, if PTF12dam is an engine-driven stellar explosion, the jet never successfully broke out from the stellar envelope, in close analogy to the picture recently suggested for the relativistic SNe 2009bb and 2012ap (Margutti et al. 2014 and references therein).

To conclude, the analysis of our deep X-ray limits in the context of GRB afterglows simulations and the recent finding of similarity in the nebular emission from SN2015bn with engine-driven SNe, suggest that either SLSNe-I are powered by very energetic collimated GRB-like outflows that were pointing far away from our line of sight ( $\theta_{obs} > 30^\circ$ ), or that SLSNe-I harbor failed jets that do not successfully break through the stellar envelope and are associated with weak X-ray emission. Late-time radio observations of SN2015bn (Nicholl et al. 2016b) argue against the off-axis relativistic jet scenario. However, the association of SN2011kl with GRB111209A clearly implies that at least some SLSNe-I harbor relativistic jets. We therefore propose that, in strict analogy to H-stripped core-collapse SNe of ordinary luminosity (e.g. Xu et al. 2008; Mazzali et al. 2008; Lazzati et al. 2012; Margutti et al. 2014), SLSNe-I are also characterized by a continuum of jets strengths and life-time of the central engine.

### 5.2. Constraints on magnetar central engines: the Ionization Break out

We compute the ionization breakout time and the X-ray luminosity at breakout following Metzger et al. (2014) and Metzger & Piro (2014). We consider a central engine with an UV/X-ray luminosity  $L$  that releases an energy  $L \times t$  in ionizing radiation on a timescale  $t$ . The radiation ionizes its way through the ejecta on a timescale

$$t_{ion} \approx \begin{cases} 120 \text{ d } M_3^{3/4} v_9^{-5/4} T_5^{-0.2} \left(\frac{X_A}{0.1}\right)^{1/4} \left(\frac{Lt}{10^{52} \text{ erg}}\right)^{-1/4} Z_8^{3/4}, (\eta_{thr} \ll 1) \\ 110 \text{ d } M_3 v_9^{-3/2} T_5^{-0.4} \left(\frac{X_A}{0.1}\right)^{1/2} \left(\frac{Lt}{10^{52} \text{ erg}}\right)^{-1/2} Z_8^{3/2}, (\eta_{thr} \gg 1), \end{cases}$$

<sup>15</sup> Note that Nicholl et al. (2016a) assume an ISM-like medium and larger  $\epsilon_B = 0.1$  and  $\theta_j = 10^\circ$ .

where  $M_3 \equiv M_{ej}/(3M_\odot)$ ,  $T_5 = T/10^5 \text{ K}$  is the temperature of electrons in the recombination layer,  $v_9 \equiv v/10^9 \text{ cm s}^{-1}$ ,  $X_Z$  is the mass fraction  $X_Z$  of elements with atomic number  $Z = 8Z_8$  in the ejecta and

$$\eta_{thr} \approx 0.7 \left(\frac{Lt}{10^{52} \text{ erg}}\right)^{-1} M_3 v_9^{-1} \left(\frac{X_A}{0.1}\right) T_5^{-0.8} Z_8^3 \quad (2)$$

is the ratio of absorptive and scattering opacity in the ejecta (Metzger et al. 2014). The spin-down timescale  $t_{sd}$  of a magnetar central engine is given by

$$t_{sd} \sim 4.7 \text{ dB}_{14}^{-2} P_{ms}^2 \quad (3)$$

and the spin-down luminosity is given by

$$L_{sd} = 5 \times 10^{46} B_{14}^2 P_{ms}^{-4} \left(1 + \frac{t}{t_{sd}}\right)^{-2} \text{ erg s}^{-1} \approx 1.1 \times 10^{48} B_{14}^{-2} t_d^{-2} \text{ erg s}^{-1} \quad (4)$$

for  $t \gg t_{sd}$ ,  $B_{14} \equiv B/10^{14} \text{ G}$ ,  $P_{ms} \equiv P/\text{ms}$ ,  $t_d \equiv t/\text{days}$  and we adopted the vacuum dipole spin-down convention employed by Kasen & Bildsten (2010). For  $L = L_{sd}$  and  $t \gg t_{sd}$  the ionization time scale of Eq. 1 can be written as follows:

$$t_{ion} \approx \begin{cases} 280 \text{ d } M_3 v_9^{-5/3} T_5^{-4/15} \left(\frac{X_A}{0.1}\right)^{1/3} B_{14}^{2/3} Z_8, (\eta_{thr} \ll 1) \\ 1273 \text{ d } M_3 v_9^{-3} T_5^{-4/5} \left(\frac{X_A}{0.1}\right) B_{14}^2 Z_8^3, (\eta_{thr} \gg 1), \end{cases} \quad (5)$$

The X-ray luminosity at ionization breakout is  $L_x \approx L_{sd}(t_{ion})/14$ . In the following we assume that Oxygen ( $Z_8 = 1$ ) dominates the bound-free opacity in the  $\sim \text{keV}$  X-ray band, we use an electron temperature  $T = 10^5 \text{ K}$ ,  $X_A = 0.1$ , velocity of the order of  $10^9 \text{ cm/s}$  and we compute the ionization time scale and the X-ray luminosity at break out and compare to our X-ray limits and measurements.

For SLSNe-I with well constrained optical bolometric emission, we use the magnetar parameters  $M_{ej}$ ,  $P$  and  $B$  that best fit the optical bolometric luminosity to estimate  $t_{ion}$  and  $L_x(t_{ion})$  (Table 4). From Table 4 and Fig. 2-4 it is clear that most of the  $L_x(t_{ion})$  are too faint to be detected and that  $t_{ion}$  is usually much larger than the  $\sim 2000$  days that we cover with our observations. However, it is also clear that  $t_{ion}$  and  $L_x(t_{ion})$  are very sensitive to the magnetar parameters and qualify as excellent probes of central engines in SLSNe-I. Magnetar central engines that would produce very similar optical bolometric outputs that cannot be distinguished with current optical-UV photometry, are instead clearly differentiated in their  $L_x(t_{ion}) - t_{ion}$  properties. As an example, for the best fitting magnetar parameters of SN2015bn in Fig. 4,  $L_x(t_{ion})$  spans  $\sim 5$  orders of magnitude and  $t_{ion}$  ranges from 0.6–88 yrs. For this SLSN-I, our deep X-ray limits obtained with XMM and the combined limit from *Swift*-XRT favor models with  $P > 2 \text{ ms}$ . The fastest spinning magnetar model with  $P = 1.5 \text{ ms}$  and relatively small ejecta mass  $M_{ej} = 7.4 M_\odot$  from Nicholl et al. (2016b) predicts  $L_x(t_{ion}) > 10^{43} \text{ erg s}^{-1}$  at  $t_{ion} \sim 0.6 \text{ yrs}$  and it is therefore disfavored by our X-ray observations (Fig. 4).

Figure 9 shows how the X-ray observations from our sample compare to the predictions from the magnetar ionization breakout model. We investigate a wide range of central engine parameters  $P = 1$ –7 ms and  $B_{14} = 0.2$ –10 G for ejecta masses  $M_{ej} = 1$ –20  $M_\odot$ . Current X-ray observations are not sensitive to magnetars with  $B_{14} \geq 2$  (Fig. 9). For  $B_{14} < 2$ , observations favor models with larger ejecta mass: for  $B_{14} = 0.2, 0.5, 1.0 \text{ G}$  the allowed parameter space is  $M_{ej} > 20, 7, 3 M_\odot$ . X-ray observations indicate that if a magnetar central engine powers

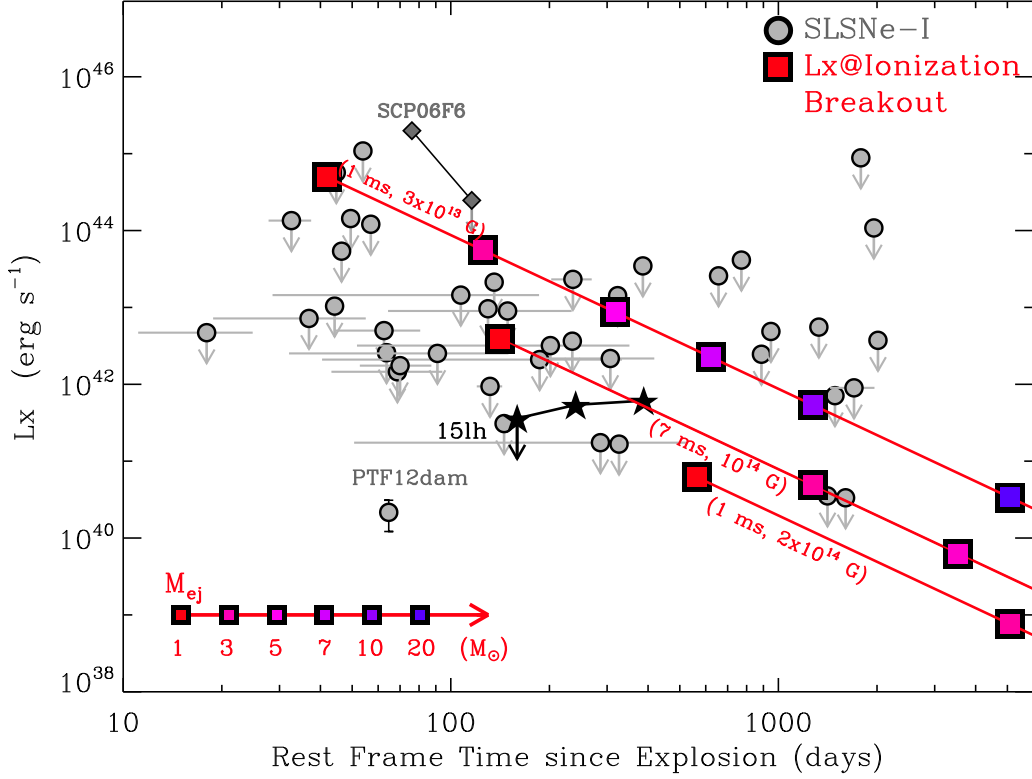


FIG. 9.— X-ray luminosity at the time of ionization break out (thick red line) for a variety of representative magnetar parameters,  $P = 1$  ms,  $B = 3 \times 10^{13}$  G (upper line),  $P = 7$  ms,  $B = 10^{14}$  G (middle line),  $P = 1$  ms,  $B = 2 \times 10^{14}$  G (lower line), and for a range of ejecta mass values  $M_{ej}$  between 1 and  $20 M_{\odot}$ . These calculations assume an Oxygen dominated ejecta composition ( $Z_8 = 1$ ),  $v = 10^9$  cm/s,  $T = 10^5$  K,  $X_A = 0.1$ . Our limits (grey dots) rule out the fastest spinning magnetars with  $P \leq 7$  ms,  $B \leq 10^{14}$  G and small ejecta masses  $M_{ej} \leq 5 M_{\odot}$ . However, we are not sensitive to magnetars with  $B_{14} \geq 2 \times 10^{14}$  G. Grey diamonds: X-ray emission at the location of SCP06F6 (Levan et al. 2013). Black stars: X-ray emission at the location of ASASSN-15lh (Margutti et al. 2017b).

the emission from SLSNe-I then it has to be either associated with a large magnetic field or with a large explosion ejecta mass. These results are independent from (but in agreement with) the values inferred from the modeling of the optical emission from SLSNe-I (Tab. 4, Nicholl et al. 2013; Inserra et al. 2013).

We end by noting that our analytic treatment of ionization break-out from the supernova ejecta requires confirmation by a more detailed photo-ionization calculation in future work, as well as a more accurate model for the spectral energy distribution of the young pulsar wind nebula. Also, by adopting a relatively low mass fraction of  $X_Z \approx 0.1$  of CNO elements (which contribute most of the bound-free opacity in the keV range) we may be underestimating the ionization break-out time and thus over-estimating the associated X-ray luminosity if the true mass fraction is higher. On the other hand, asphericity in the ejecta (e.g. along the rotation axis) would reduce the break-out time along directions of lower than average density and introduce a viewing angle dependence to the emission. An extension from an analytical 1D model (used here) to detailed multi-D formulations is indeed necessary to fully characterize the expected X-ray signature from ionization breakout, and possibly solve the current tension between the anticipated vs. observed spectral features and their evolution in the magnetar model (e.g. Liu & Modjaz 2016).

## 6. SUMMARY AND CONCLUSIONS

We present the results from an extensive systematic survey of X-ray emission from 26 hydrogen-stripped SLSNe in the local Universe with *Swift*, Chandra and XMM. These data

cover the SLSNe-I evolution from  $\sim$  days until 2000 days (rest-frame) since explosion, reaching  $L_x \sim 10^{40}$  erg s $^{-1}$ . The unprecedented depth of these observations provided the deepest limits on the X-ray emission from SLSNe-I to date and enabled the detection of X-ray emission at the location of the slowly evolving SLSN-I PTF12dam. The major results from our investigation can be summarized as follows:

- Superluminous X-ray emission  $L_x \sim 10^{45}$  erg s $^{-1}$  of the kind detected at the location of SCP06F6 is *not* a common trait of SLSNe-I. Superluminous X-ray emission requires peculiar physical conditions that are likely not shared by the majority of SLSNe-I. If present, its duration is  $\leq 2$  months at  $t < 2000$  days and  $\leq$  few days at earlier epochs  $t < 100$  days (Fig. 5).
- We place sensitive limits on the sub-pc environments of the SLSNe-I with deepest observations and constrain pre-explosion mass-loss history their stellar progenitors of SLSNe-I (Fig. 6-7). The most sensitive X-ray observations in our sample rule out the densest environments typical of LBV eruptions and type-IIIn SNe. For PTF12dam, the observations point to a clean environment similar to engine-driven SNe and argue against the dense CSM typical of extended stellar progenitors like RSG. Observations indicate  $\dot{M} < 2 \times 10^{-5} M_{\odot} \text{yr}^{-1}$ . This result suggests that CSM interaction is unlikely to play a key role in the process that powers the luminous display in some SLSNe-I and that at least some SLSN-I progenitors end their life as compact stars surrounded by a low-density medium.



- We do not find compelling observational evidence for relativistic outflows in SLSNe-I. SLSNe-I might either be powered by energetic relativistic GRB-like outflows that we did not detect because pointed far away from our line of sight ( $\theta_{\text{obs}} > 30^\circ$ ), or might harbor failed jets that do not successfully pierce through the stellar envelope. Deep X-ray observations of PTF12dam rule out even the weakest emission from uncollimated GRB outflows (Fig. 8), suggesting that *if* PTF12dam is a jet-driven explosion, then the jet never successfully broke out from the surface (in close similarity to the relativistic SNe 2009bb and 2012ap). However, the SLSN-I 2011kl was found in association with the fully-relativistic, fully-successful jet of GRB111209A. We thus propose that, just like H-stripped core-collapse SN, SLSNe-I might also be characterized by a continuum of jet power and central-engine life-times.
- The X-ray ionization break out is a very sensitive probe of the properties of a hidden magnetar central engine in SLSNe-I. Magnetar central engines that would produce very similar optical/UV displays are instead clearly differentiated in terms of X-ray luminosities and time scales of the ionization break out (Fig. 3-4). Current X-ray observations indicate that *if* a magnetar central engine powers SLSNe-I, then it has to be either associated with a large magnetic field  $B_{14} > 2$  G or large ejecta mass ( $M_{ej} > 20, 7, 3 M_\odot$  for  $B_{14} = 0.2, 0.5, 1.0$  G).

This X-ray campaign provided constraints on the sub-pc environment and properties of central engines in SLSNe-I. To further advance our knowledge and understanding of SLSNe-I it is necessary to systematically explore the region of the parameter space with  $L_x < 10^{41} \text{ erg s}^{-1}$  both at very early ( $t < 30$

days, rest-frame) and late times ( $t > 1000$  days, rest-frame), where the emission from an off-axis relativistic jet, weak uncollimated relativistic outflow or magnetar ionization break-out might be found. This parameter space is almost an entirely uncharted territory of exploration and holds promise for future discoveries.

This research has made use of the XRT Data Analysis Software (XRTDAS) developed under the responsibility of the ASI Science Data Center (ASDC), Italy. We acknowledge the use of public data from the Swift data archive. This work is partially based on data acquired with the Swift GO program 1114109 (grant NNX16AT51G, PI Margutti). The scientific results reported in this article are partially based on observations made by the Chandra X-ray Observatory under program GO6-17052A, PI Margutti, observations IDs 17879, 17880, 17881, 17882 and IDs 13772, 14444, 14446, (PI Pooley). Partially based on observations by XMM-Newton, IDs 0743110301, 0743110701, 0770380201, 0770380401, PI Margutti, proposal 74311. CG acknowledges University of Ferrara for use of the local HPC facility co-funded by the “Large-Scale Facilities 2010” project (grant 7746/2011). Development of the Boxfit code was supported in part by NASA through grant NNX10AF62G issued through the Astrophysics Theory Program and by the NSF through grant AST-1009863. Simulations for BOXFIT version 2 have been carried out in part on the computing facilities of the Computational Center for Particle and Astrophysics (C2PAP) of the research cooperation “Excellence Cluster Universe” in Garching, Germany. G.M. acknowledges the financial support from the UnivEarthS Labex program of Sorbonne Paris Cité (ANR10LABX0023 and ANR11IDEX000502).

## REFERENCES

- Angus, C. R., Levan, A. J., Perley, D. A., et al. 2016, *MNRAS*, **458**, 84
- Barbary, K., Dawson, K. S., Tokita, K., et al. 2009, *ApJ*, **690**, 1358
- Baumont, S., Le Guillou, L., Le Breton, R., et al. 2015, The Astronomer’s Telegram, 8369
- Benetti, S., Nicholl, M., Cappellaro, E., et al. 2014, *MNRAS*, **441**, 289
- Berger, E., Kulkarni, S. R., & Chevalier, R. A. 2002, *ApJ*, **577**, L5
- Bersten, M. C., Benvenuto, O. G., Orellana, M., & Nomoto, K. 2016, *ApJ*, **817**, L8
- Björnsson, C.-I., & Fransson, C. 2004, *ApJ*, **605**, 823
- Campbell, H., Walton, N., Blagorodnova, N., et al. 2014, The Astronomer’s Telegram, 6524
- Chakraborti, S., Soderberg, A., Chomiuk, L., et al. 2015, *ApJ*, **805**, 187
- Challis, P., Kirshner, R., Mandel, K., et al. 2016, The Astronomer’s Telegram, 8952
- Chatzopoulos, E., Wheeler, J. C., Vinko, J., et al. 2016, ArXiv e-prints, [arXiv:1603.06926 \[astro-ph.HE\]](https://arxiv.org/abs/1603.06926)
- Chen, T.-W., Smartt, S. J., Bresolin, F., et al. 2013, *ApJ*, **763**, L28
- Chen, T.-W., Smartt, S. J., Jerkstrand, A., et al. 2015, *MNRAS*, **452**, 1567
- Chen, T.-W., Nicholl, M., Smartt, S. J., et al. 2016, ArXiv e-prints, [arXiv:1611.09910 \[astro-ph.HE\]](https://arxiv.org/abs/1611.09910)
- Chevalier, R. A., & Fransson, C. 2006, *ApJ*, **651**, 381
- Chevalier, R. A., & Irwin, C. M. 2011, *ApJ*, **729**, L6
- Chomiuk, L., Chornock, R., Soderberg, A. M., et al. 2011, *ApJ*, **743**, 114
- Chornock, R., Bhirimbhakti, K., Katebi, R., et al. 2016, The Astronomer’s Telegram, 8790
- Corsi, A., Ofek, E. O., Gal-Yam, A., et al. 2014, *ApJ*, **782**, 42
- Crowther, P. A. 2007, *ARA&A*, **45**, 177
- Dai, L., McKinney, J. C., & Miller, M. C. 2015, *ApJ*, **812**, L39
- Dai, Z. G., Wang, S. Q., Wang, J. S., Wang, L. J., & Yu, Y. W. 2016, *ApJ*, **817**, 132
- D’Andrea, C., Smith, M., Sullivan, M., et al. 2015, The Astronomer’s Telegram, 8092
- de Jager, C., Nieuwenhuijzen, H., & van der Hucht, K. A. 1988, *A&AS*, **72**, 259
- Dimitriadis, G., Firth, R., Frohmaier, C., et al. 2016, The Astronomer’s Telegram, 8555
- Dong, S., Shappee, B. J., Prieto, J. L., et al. 2016, *Science*, **351**, 257
- Drake, A. J., Djorgovski, S. G., Mahabal, A. A., et al. 2012, The Astronomer’s Telegram, 3873
- . 2013, Central Bureau Electronic Telegrams, 3460
- Drout, M. R., Milisavljevic, D., Parrent, J., et al. 2016, *ApJ*, **821**, 57
- Fransson, C., & Björnsson, C.-I. 1998, *ApJ*, **509**, 861
- Gal-Yam, A. 2012, *Science*, **337**, 927
- Gal-Yam, A., Mazzali, P., Ofek, E. O., et al. 2009, *Nature*, **462**, 624
- Gänsicke, B. T., Levan, A. J., Marsh, T. R., & Wheatley, P. J. 2009, *ApJ*, **697**, L129
- Godoy-Rivera, D., Stanek, K. Z., Kochanek, C. S., et al. 2016, ArXiv e-prints, [arXiv:1605.00645 \[astro-ph.HE\]](https://arxiv.org/abs/1605.00645)
- Greiner, J., Mazzali, P. A., Kann, D. A., et al. 2015, *Nature*, **523**, 189
- Insera, C., Smartt, S. J., Jerkstrand, A., et al. 2013, *ApJ*, **770**, 128
- Insera, C., Nicholl, M., Chen, T.-W., et al. 2017, ArXiv e-prints, [arXiv:1701.00941 \[astro-ph.HE\]](https://arxiv.org/abs/1701.00941)
- Jerkstrand, A., Smartt, S. J., Insera, C., et al. 2016, ArXiv e-prints, [arXiv:1608.02994 \[astro-ph.HE\]](https://arxiv.org/abs/1608.02994)
- Kalberla, P. M. W., Burton, W. B., Hartmann, D., et al. 2005, *A&A*, **440**, 775
- Kamble, A., Soderberg, A. M., Chomiuk, L., et al. 2014, *ApJ*, **797**, 2
- Kamble, A., Margutti, R., Soderberg, A. M., et al. 2016, *ApJ*, **818**, 111
- Kangas, T., Dennefeld, M., Harmanen, J., et al. 2015, The Astronomer’s Telegram, 8296
- Kasen, D., & Bildsten, L. 2010, *ApJ*, **717**, 245



- Kostrzewa-Rutkowska, Z., Wyrzykowski, L., Kozłowski, S., et al. 2015, *The Astronomer's Telegram*, 8314
- Kouveliotou, C., Woosley, S. E., Patel, S. K., et al. 2004, *ApJ*, **608**, 872
- Kozyreva, A., Hirschi, R., Blinnikov, S., & den Hartogh, J. 2016, *MNRAS*, **459**, L21
- Krauss, M. I., Soderberg, A. M., Chomiuk, L., et al. 2012, *ApJ*, **750**, L40
- Lazzati, D., Morsony, B. J., Blackwell, C. H., & Begelman, M. C. 2012, *ApJ*, **750**, 68
- Leget, P.-F., Guillou, L. L., Fleury, M., et al. 2014, *The Astronomer's Telegram*, 5718
- Leloudas, G., Patat, F., Maund, J. R., et al. 2015a, *ApJ*, **815**, L10
- Leloudas, G., Schulze, S., Krühler, T., et al. 2015b, *MNRAS*, **449**, 917
- Leloudas, G., Fraser, M., Stone, N. C., et al. 2016, ArXiv e-prints, [arXiv:1609.02927](https://arxiv.org/abs/1609.02927) [astro-ph.HE]
- Levan, A. J., Read, A. M., Metzger, B. D., Wheatley, P. J., & Tanvir, N. R. 2013, *ApJ*, **771**, 136
- Liu, Y.-Q., & Modjaz, M. 2016, ArXiv e-prints, [arXiv:1612.07321](https://arxiv.org/abs/1612.07321) [astro-ph.HE]
- Lunnan, R., Chornock, R., Berger, E., et al. 2014, *ApJ*, **787**, 138
- . 2015, *ApJ*, **804**, 90
- . 2016, *ApJ*, **831**, 144
- Margutti, R., Soderberg, A. M., Chomiuk, L., et al. 2012, *ApJ*, **751**, 134
- Margutti, R., Zaninoni, E., Bernardini, M. G., et al. 2013a, *MNRAS*, **428**, 729
- Margutti, R., Soderberg, A. M., Wieringa, M. H., et al. 2013b, *ApJ*, **778**, 18
- Margutti, R., Milisavljevic, D., Soderberg, A. M., et al. 2014, *ApJ*, **797**, 107
- Margutti, R., Kamble, A., Milisavljevic, D., et al. 2017a, *ApJ*, **835**, 140
- Margutti, R., Metzger, B. D., Chornock, R., et al. 2017b, *ApJ*, **836**, 25
- Marshall, J. R., van Loon, J. T., Matsuura, M., et al. 2004, *MNRAS*, **355**, 1348
- Massey, P., Neugent, K. F., & Morrell, N. 2015, *ApJ*, **807**, 81
- Mazzali, P. A., Valenti, S., Della Valle, M., et al. 2008, *Science*, **321**, 1185
- Metzger, B. D., Margalit, B., Kasen, D., & Quataert, E. 2015, *MNRAS*, **454**, 3311
- Metzger, B. D., & Piro, A. L. 2014, *MNRAS*, **439**, 3916
- Metzger, B. D., Vurm, I., Hascoët, R., & Beloborodov, A. M. 2014, *MNRAS*, **437**, 703
- Milisavljevic, D., Soderberg, A. M., Margutti, R., et al. 2013, *ApJ*, **770**, L38
- Mineo, S., Gilfanov, M., & Sunyaev, R. 2012, *MNRAS*, **426**, 1870
- Nicholl, M., Berger, E., Margutti, R., et al. 2017, *ApJ*, **835**, L8
- Nicholl, M., Smartt, S. J., Jerkstrand, A., et al. 2013, *Nature*, **502**, 346
- . 2014, *MNRAS*, **444**, 2096
- Nicholl, M., Berger, E., Smartt, S. J., et al. 2016a, *ApJ*, **826**, 39
- Nicholl, M., Berger, E., Margutti, R., et al. 2016b, *ApJ*, **828**, L18
- Ofek, E. O., Cameron, P. B., Kasliwal, M. M., et al. 2007, *ApJ*, **659**, L13
- Ofek, E. O., Zoglauer, A., Boggs, S. E., et al. 2014, *ApJ*, **781**, 42
- Pastorello, A., Smartt, S. J., Botticella, M. T., et al. 2010, *ApJ*, **724**, L16
- Perley, D. A., Quimby, R. M., Yan, L., et al. 2016, *ApJ*, **830**, 13
- Pian, E., Amati, L., Antonelli, L. A., et al. 2000, *ApJ*, **536**, 778
- Quimby, R. M., Gal-Yam, A., Arcavi, I., et al. 2011a, *The Astronomer's Telegram*, 3841
- Quimby, R. M., Sternberg, A., & Matheson, T. 2011b, *The Astronomer's Telegram*, 3344
- Quimby, R. M., Kulkarni, S. R., Kasliwal, M. M., et al. 2011c, *Nature*, **474**, 487
- Roming, P. W. A., Pritchard, T. A., Brown, P. J., et al. 2009, *ApJ*, **704**, L118
- Ryder, S. D., Sadler, E. M., Subrahmanyan, R., et al. 2004, *MNRAS*, **349**, 1093
- Schulze, S., Krühler, T., Leloudas, G., et al. 2016, ArXiv e-prints, [arXiv:1612.05978](https://arxiv.org/abs/1612.05978)
- Sironi, L., Keshet, U., & Lemoine, M. 2015, *Space Sci. Rev.*, **191**, 519
- Smartt, S. J., Wright, D., Valenti, S., et al. 2012, *The Astronomer's Telegram*, 3918
- Smith, M., Firth, R., Dimitriadis, G., et al. 2014, *The Astronomer's Telegram*, 6739
- Smith, N. 2014, *ARA&A*, **52**, 487
- Smith, N., & McCray, R. 2007, *ApJ*, **671**, L17
- Smith, N., & Owocki, S. P. 2006, *ApJ*, **645**, L45
- Smith, N., Li, W., Foley, R. J., et al. 2007, *ApJ*, **666**, 1116
- Soderberg, A. M., Brunthaler, A., Nakar, E., Chevalier, R. A., & Bietenholz, M. F. 2010a, *ApJ*, **725**, 922
- Soderberg, A. M., Kulkarni, S. R., Berger, E., et al. 2005, *ApJ*, **621**, 908
- Soderberg, A. M., Nakar, E., Berger, E., & Kulkarni, S. R. 2006a, *ApJ*, **638**, 930
- Soderberg, A. M., Kulkarni, S. R., Nakar, E., et al. 2006b, *Nature*, **442**, 1014
- Soderberg, A. M., Berger, E., Page, K. L., et al. 2008, *Nature*, **453**, 469
- Soderberg, A. M., Chakraborti, S., Pignata, G., et al. 2010b, *Nature*, **463**, 513
- Sukhbold, T., & Woosley, S. E. 2016, *ApJ*, **820**, L38
- Thöne, C. C., de Ugarte Postigo, A., García-Benito, R., et al. 2015, *MNRAS*, **451**, L65
- van Dyk, S. D., Weiler, K. W., Sramek, R. A., Rupen, M. P., & Panagia, N. 1994, *ApJ*, **432**, L115
- van Eerten, H., van der Horst, A., & MacFadyen, A. 2012, *ApJ*, **749**, 44
- van Loon, J. T., Cioni, M.-R. L., Zijlstra, A. A., & Loup, C. 2005, *A&A*, **438**, 273
- van Putten, M. H. P. M., & Della Valle, M. 2016, ArXiv e-prints, [arXiv:1610.00535](https://arxiv.org/abs/1610.00535) [astro-ph.HE]
- Vinko, J., Zheng, W., Romadan, A., et al. 2010, *Central Bureau Electronic Telegrams*, 2556
- Vinko, J., Zheng, W., Pandey, S. B., et al. 2012, in *American Astronomical Society Meeting Abstracts*, Vol. 219, American Astronomical Society Meeting Abstracts #219, 436.04
- Vreeswijk, P. M., Leloudas, G., Gal-Yam, A., et al. 2017, *ApJ*, **835**, 58
- Wang, S. Q., Liu, L. D., Dai, Z. G., Wang, L. J., & Wu, X. F. 2015, ArXiv e-prints, [arXiv:1509.05543](https://arxiv.org/abs/1509.05543) [astro-ph.HE]
- . 2016, *ApJ*, **828**, 87
- Watson, D., Hjorth, J., Levan, A., et al. 2004, *ApJ*, **605**, L101
- Weiler, K. W., Panagia, N., Montes, M. J., & Sramek, R. A. 2002, *ARA&A*, **40**, 387
- Woosley, S. E. 2010, *ApJ*, **719**, L204
- Xu, D., Watson, D., Fynbo, J., et al. 2008, in *COSPAR Meeting*, Vol. 37, 37th COSPAR Scientific Assembly, 3512
- Yan, L., Quimby, R., Ofek, E., et al. 2015, *ApJ*, **814**, 108
- Yan, L., Quimby, R., Gal-Yam, A., et al. 2016, ArXiv e-prints, [arXiv:1611.02782](https://arxiv.org/abs/1611.02782) [astro-ph.SR]

## APPENDIX

## X-RAY OBSERVATIONS OF SLSNE-I

We provide here the details about the X-ray observations of SLSNe-I in the “bronze” and “iron” samples. Table 5 reports the measured fluxes for the entire sample of 26 SLSNe-I analyzed in this paper. For the non-detections we assume a non-thermal power-law spectrum with photon index  $\Gamma = 2$  and Galactic absorption.

*SN2009jh/PTF09cwl*

*Swift*-XRT observed SN2009jh (Quimby et al. 2011c) on 2009 August 29 until 2016 Sep 25 ( $\delta t = 48 - 1961$  days rest-frame since explosion). No X-ray source is detected at the location of the supernova. With respect to Levan et al. (2013) we add the late-time data-set acquired in 2016.

*PTF09atu*

*Swift*-XRT observed PTF09atu (Quimby et al. 2011c) on 2009 August 19 until 2016 October 6 ( $\delta t = 49 - 1785$  days rest-frame since explosion). No X-ray source is detected at the location of the supernova. With respect to Levan et al. (2013) we add the late-time data-set acquired in 2016.

*PTF09cnd*

*Swift*-XRT started observing PTF09cnd (Quimby et al. 2011c) on 2014 August 8 until October 3 ( $\delta t = 1487 - 1531$  days rest-frame since explosion, exposure time of 26 ks). This data set has been presented by Levan et al. (2013). The location of PTF09cnd was serendipitously observed by *Swift* between 2016 February 4 and September 23 ( $\delta t = 1921 - 2104$  days rest-frame since explosion, exposure time of 62 ks). No X-ray source is detected at the location of the supernova. XMM observed the location of PTF09cnd on 2014 August 8 ( $\delta t = 1487$  days rest-frame since explosion). The net exposure time is 27.7 ks (EPIC-pn data). No source is detected and we derive a  $3\sigma$  count-rate upper limit of  $1.5 \times 10^{-3} \text{ cs}^{-1}$  (0.3 -10 keV), which corresponds to an absorbed (unabsorbed) flux  $< 3.2 \times 10^{-15} \text{ erg s}^{-1} \text{ cm}^{-2}$  ( $< 3.4 \times 10^{-15} \text{ erg s}^{-1} \text{ cm}^{-2}$ ).

*PTF10aagc*

*Swift*-XRT observed PTF10aagc (Yan et al. 2015) on 2010 Nov 08 ( $\delta t = 79$  days rest-frame since explosion). No X-ray source is detected at the location of the supernova.

*SN2010md/PTF10hgi*

*Swift*-XRT started observing PTF10hgi (Inserra et al. 2013) on 2010 July 13 until 2010 July 18 ( $\delta t = 61 - 66$  days rest-frame since explosion). No X-ray source is detected at the location of the supernova as reported by Levan et al. (2013).

*SN2010gx/CSS100313/PTF10cwr*

*Swift*-XRT started observing SN2010gx (Pastorello et al. 2010; Quimby et al. 2011c; Chen et al. 2013; Inserra et al. 2013; Perley et al. 2016) on 2010 March 19 until 2012 May 14 ( $\delta t = 19 - 659$  days rest-frame since explosion). A portion of this data set has been presented by Levan et al. (2013). Here we add the observations acquired in 2012. No X-ray source is detected at the location of the supernova.

*SN2010kd*

*Swift*-XRT started observing SN2010kd (Vinko et al. 2010, 2012) on 2010 Nov 30 until 2016 June 21 ( $\delta t = 120 - 1964$  days rest-frame since explosion). With respect to Levan et al. (2013), here we include late-time data acquired in 2014 and 2016. No X-ray source is detected at the location of the supernova.

*SN2011ke/CSS110406/PTF11dij*

*Swift*-XRT started observing SN2011ke (Quimby et al. 2011b; Drake et al. 2013; Perley et al. 2016) on 2011 May 14 until 2012 April 12 ( $\delta t = 40 - 332$  days rest-frame since explosion), as reported by Levan et al. (2013). No X-ray source is detected at the location of the supernova.

The CXO serendipitously imaged the sky location of SN2011ke on August 28, 2015 ( $\delta t = 1411$  days rest-frame since explosion, exposure time of 56 ks) and on April 4, 2016 ( $\delta t = 1604$  days rest-frame since explosion, exposure time of 59 ks). These data are presented here for the first time. No X-ray source is detected at the location of SN2011ke and we infer a  $3\sigma$  count-rate upper limit  $< 5.4 \times 10^{-5} \text{ cs}^{-1}$  and  $< 5.1 \times 10^{-5} \text{ cs}^{-1}$  in the 0.5-8 keV energy band, for the first and second epoch, respectively. For a non-thermal power-law spectrum with index  $\Gamma = 2$  these results translate into unabsorbed 0.3-10 keV flux limits of  $< 6.4 \times 10^{-16} \text{ erg s}^{-1} \text{ cm}^{-2}$  and  $< 6.0 \times 10^{-16} \text{ erg s}^{-1} \text{ cm}^{-2}$ .

*PS1-11bdn*

*Swift*-XRT started observing PS1-11bdn (Lunnan et al. 2014, 2015; Schulze et al. 2016) on 2012 January 11 until 2012 January 28 ( $\delta t = 28 - 35$  days rest-frame since explosion). No X-ray source is detected at the location of the supernova.

*PTF11rks/SN2011kg*

*Swift*-XRT started observing PTF11rks (Quimby et al. 2011a; Inserra et al. 2013; Perley et al. 2016) on 2011 December 30 until 2012 January 15 ( $\delta t = 11 - 25$  days rest-frame since explosion), as reported by Levan et al. (2013). No X-ray source is detected at the location of the supernova.

*SN2012il/PS1-12fo/CSS120121*

*Swift*-XRT started observing SN2012il (Drake et al. 2012; Smartt et al. 2012; Inserra et al. 2013; Lunnan et al. 2014) on 2012 Feb 13 until 2016 June 25 ( $\delta t = 44 - 1400$  days rest-frame since explosion). No X-ray source is detected at the location of the supernova. With respect to Levan et al. (2013) we add here the 2016 data-set.

*DES15C3hav*

*Swift*-XRT started observing DES15C3hav (Challis et al. 2016) on 2016 June 12 until 2016 Sep 13 ( $\delta t = 202 - 269$  days rest-frame since explosion). No X-ray source is detected at the location of the supernova.

*iPTF13ehe*

*Swift*-XRT observed iPTF13ehe (Yan et al. 2015; Wang et al. 2015) on 2014 December 23 ( $\delta t = 385$  days rest-frame since explosion). No X-ray source is detected at the location of the supernova.

*LSQ14an*

*Swift*-XRT started observing LSQ14an (Leget et al. 2014; Jerkstrand et al. 2016; Inserra et al. 2017) on 2014 March 24 until 2014 December 8, with a final observation taken on 2016 August 8 ( $\delta t = 196 - 949$  days rest-frame since explosion). A portion of the data set has been presented in Inserra et al. (2017). Here we present the complete data set of X-ray observations available on LSQ14an.

*LSQ14fxj*

*Swift*-XRT started observing LSQ14fxj (Smith et al. 2014; Schulze et al. 2016) on 2014 October 29 until 2015 June 16 ( $\delta t = 64 - 234$  days rest-frame since explosion). No X-ray source is detected at the location of the supernova.

*LSQ14mo*

*Swift*-XRT started observing LSQ14mo (Leloudas et al. 2015a; Chen et al. 2016) on 2014 January 31, with a last observation taken on 2016 July 24 ( $\delta t = 52 - 774$  days rest frame since explosion). No X-ray source is detected at the location of the supernova.

*CSS140925-005854*

*Swift*-XRT started observing CSS140925-005854 (Campbell et al. 2014; Schulze et al. 2016) on 2014 October 11 until 2015 May 29 ( $\delta t = 29 - 186$  days rest-frame since explosion). No X-ray source is detected at the location of the supernova.

*DES15S2nr*

*Swift*-XRT started observing DES15S2nr (D’Andrea et al. 2015) on 2015 September 25 until 2016 February 15m with another observation acquired on 2016 Sep 14 ( $\delta t = 32 - 323$  days res-frame since explosion). No X-ray source is detected at the location of the supernova.

*OGLE15qz*

*Swift*-XRT observed OGLE15qz (Kangas et al. 2015; Kostrzewa-Rutkowska et al. 2015) on 2015 November 25 ( $\delta t = 54$  days rest-frame since explosion). No X-ray source is detected at the location of the supernova.

*OGLE15sd*

*Swift*-XRT started observing OGLE15sd (Baumont et al. 2015) on 2015 December 8 until 2015 December 9 ( $\delta t = 34 - 212$  days rest-frame since explosion). No X-ray source is detected at the location of the supernova.

*PS16aqv*

*Swift*-XRT started observing PS16aqv (Chornock et al. 2016) on 2016 March 9 until 2016 June 10 ( $\delta t = 53 - 131$  days rest-frame since explosion). No X-ray source is detected at the location of the supernova.

*PS16op*

*Swift*-XRT observed PS16op (Dimitriadis et al. 2016) on 2016 January 20 ( $\delta t = 57$  days rest-frame since explosion). No X-ray source is detected at the location of the supernova.

TABLE 5  
X-RAY OBSERVATIONS OF SLSNE-I

SN	$t_{\text{START}}$ (MJD)	$t_{\text{STOP}}$ (MJD)	Unabsorbed Flux (0.3-10 keV) ( $10^{-14} \text{ erg s}^{-1} \text{ cm}^{-2}$ )	Instrument
SCP06F6	53949	53949	13.	XMM <sup>16</sup>
	54043	54043	< 1.40	Chandra
PTF09atu	55062.188	55062.328	< 14.50	Swift-XRT
PTF09cnd	57667.055	57667.055	< 89.37	Swift-XRT
	55061.883	55062.000	< 12.02	Swift-XRT
	55065.828	55065.945	< 12.35	Swift-XRT
	55069.016	55069.289	< 14.47	Swift-XRT
	55073.637	55073.777	< 12.43	Swift-XRT
	55077.312	55077.594	< 17.12	Swift-XRT
	55084.012	55084.887	< 13.73	Swift-XRT
	55097.812	55097.945	< 25.94	Swift-XRT
	55107.375	55107.453	< 22.40	Swift-XRT
	57422.016	57422.766	< 57.30	Swift-XRT
	57426.078	57426.406	< 41.68	Swift-XRT
	57435.129	57435.934	< 173.40	Swift-XRT
	57450.680	57450.820	< 32.82	Swift-XRT
	57456.250	57456.266	< 167.44	Swift-XRT
	57463.633	57463.977	< 37.95	Swift-XRT
	57520.109	57520.266	< 29.88	Swift-XRT
	57562.781	57562.930	< 21.62	Swift-XRT

<sup>16</sup> From Levan et al. (2013).

TABLE 5 — *Continued*

SN	$t_{START}$ (MJD)	$t_{STOP}$ (MJD)	Unabsorbed Flux (0.3–10 keV) ( $10^{-14} \text{ erg s}^{-1} \text{ cm}^{-2}$ )	Instrument
	57565.641	57565.781	< 104.19	Swift-XRT
	57568.098	57568.309	< 16.07	Swift-XRT
	57575.074	57575.418	< 11.76	Swift-XRT
	57590.371	57590.793	< 9.41	Swift-XRT
	57653.570	57653.977	< 10.31	Swift-XRT
	57654.562	57654.906	< 10.42	Swift-XRT
	56877.875	56878.250	< 0.34	XMM
SN2009jh/PTF09cwl	55072.574	55072.652	< 12.88	Swift-XRT
	57641.000	57641.016	< 55.08	Swift-XRT
	57643.477	57643.477	< 211.95	Swift-XRT
PTF10aagc	57656.555	57656.570	< 55.45	Swift-XRT
SN2010gx	55508.016	55508.094	< 15.99	Swift-XRT
	55274.141	55274.281	< 13.61	Swift-XRT
	55275.672	55275.688	< 62.42	Swift-XRT
	55280.570	55280.648	< 32.07	Swift-XRT
	55286.203	55286.469	< 33.74	Swift-XRT
	55294.086	55294.430	< 27.03	Swift-XRT
	55302.512	55302.590	< 31.56	Swift-XRT
	55309.617	55309.633	< 32.22	Swift-XRT
	55318.578	55318.656	< 19.97	Swift-XRT
	56055.809	56055.887	< 24.77	Swift-XRT
SN2010kd	56060.750	56061.297	< 35.85	Swift-XRT
	55530.133	55530.195	< 32.89	Swift-XRT
	55530.914	55530.930	< 45.20	Swift-XRT
	55546.297	55546.383	< 13.49	Swift-XRT
	55549.047	55549.133	< 18.50	Swift-XRT
	55552.387	55552.535	< 14.20	Swift-XRT
	55555.812	55555.953	< 12.21	Swift-XRT
	56980.895	56980.910	< 67.81	Swift-XRT
	56982.914	56982.914	< 187.60	Swift-XRT
	56985.430	56985.906	< 28.37	Swift-XRT
	56987.027	56988.973	< 29.46	Swift-XRT
	57388.781	57388.984	< 42.94	Swift-XRT
	57392.109	57392.781	< 22.15	Swift-XRT
	57396.367	57396.836	< 20.91	Swift-XRT
	57413.969	57413.969	< 207.18	Swift-XRT
	57469.016	57470.000	< 18.83	Swift-XRT
	57475.844	57475.844	< 204.92	Swift-XRT
	57478.109	57478.109	< 247.12	Swift-XRT
	57479.164	57479.164	< 171.40	Swift-XRT
	57489.023	57489.820	< 125.06	Swift-XRT
	57497.000	57497.000	< 93.42	Swift-XRT
	57498.590	57498.590	< 220.37	Swift-XRT
	57523.902	57523.910	< 103.97	Swift-XRT
	57525.906	57525.906	< 168.76	Swift-XRT
	57533.000	57533.000	< 260.30	Swift-XRT
	57560.129	57560.996	< 21.92	Swift-XRT
SN2010md/PTF10hgi	55390.754	55390.824	< 28.96	Swift-XRT
	55395.219	55395.297	< 16.37	Swift-XRT
SN2011ke	55695.234	55695.312	< 19.56	Swift-XRT
	55711.633	55712.039	< 9.83	Swift-XRT
	55718.668	55718.738	< 40.49	Swift-XRT
	55719.121	55719.887	< 22.74	Swift-XRT
	55720.195	55720.211	< 28.12	Swift-XRT
	55994.992	55994.992	< 1106.19	Swift-XRT
	55997.070	55998.070	< 46.63	Swift-XRT
	56000.152	56000.746	< 110.62	Swift-XRT
	56004.945	56004.961	< 57.84	Swift-XRT
	56008.445	56008.445	< 118.21	Swift-XRT
	56017.109	56017.117	< 104.83	Swift-XRT
	56020.449	56020.457	< 88.93	Swift-XRT
	56029.555	56029.555	< 354.63	Swift-XRT
	57481.375	57482.078	< 0.06	Chandra
	57262.688	57263.375	< 0.06	Chandra
PS1-11bdn	55937.477	55937.758	< 8.46	Swift-XRT
	55950.359	55950.656	< 11.36	Swift-XRT
	55953.258	55954.320	< 18.02	Swift-XRT
PTF11rks	55925.223	55925.301	< 34.22	Swift-XRT
	55927.055	55927.367	< 11.94	Swift-XRT
	55931.312	55931.938	< 15.17	Swift-XRT
	55936.203	55936.750	< 8.83	Swift-XRT
	55941.000	55941.562	< 11.41	Swift-XRT
PTF12dam	56069.836	56069.977	< 17.56	Swift-XRT
	56077.062	56077.547	< 20.73	Swift-XRT
	56085.156	56085.234	< 43.10	Swift-XRT
	56091.172	56091.188	< 25.54	Swift-XRT



TABLE 5 — *Continued*

SN	$t_{START}$ (MJD)	$t_{STOP}$ (MJD)	Unabsorbed Flux (0.3–10 keV) ( $10^{-14} \text{ erg s}^{-1} \text{ cm}^{-2}$ )	Instrument
SN2012il/PS1-12fo	56098.004	56098.066	< 23.20	Swift-XRT
	56105.398	56105.742	< 44.54	Swift-XRT
	56106.930	56106.945	< 45.62	Swift-XRT
	56112.145	56112.223	< 52.08	Swift-XRT
	56119.703	56119.781	< 16.38	Swift-XRT
	56126.320	56126.336	< 38.08	Swift-XRT
	56990.820	56990.836	< 28.84	Swift-XRT
	57006.137	57006.473	< 39.15	Swift-XRT
	57008.203	57008.812	< 43.46	Swift-XRT
	57017.992	57018.266	< 35.63	Swift-XRT
	56089.832	56097.293	$0.07 \pm 0.03$	Chandra
	55970.703	55970.734	< 23.48	Swift-XRT
	55970.992	55971.133	< 30.80	Swift-XRT
	57396.363	57396.363	< 343.90	Swift-XRT
	57442.691	57442.887	< 102.68	Swift-XRT
	57443.023	57443.023	< 339.37	Swift-XRT
	57444.270	57444.270	< 562.48	Swift-XRT
	57461.414	57461.414	< 777.65	Swift-XRT
	57469.656	57469.656	< 1468.47	Swift-XRT
	57478.430	57478.430	< 278.60	Swift-XRT
	57479.094	57480.094	< 91.73	Swift-XRT
	57519.977	57519.977	< 426.58	Swift-XRT
	57531.602	57531.875	< 26.46	Swift-XRT
	57558.855	57559.793	< 26.16	Swift-XRT
	57563.703	57564.641	< 30.80	Swift-XRT
iPTF13ehe	57014.238	57014.832	< 8.61	Swift-XRT
CSS140925-005854	56941.695	56941.914	< 9.72	Swift-XRT
	56942.289	56942.438	< 15.10	Swift-XRT
	56995.039	56995.930	< 6.30	Swift-XRT
	57032.059	57032.480	< 5.98	Swift-XRT
LSQ14an	57171.008	57171.484	< 7.09	Swift-XRT
	56740.516	56740.938	< 8.13	Swift-XRT
	56839.305	56839.570	< 39.80	Swift-XRT
	56841.031	56841.906	< 9.50	Swift-XRT
	56842.172	56842.781	< 26.84	Swift-XRT
	56846.840	56846.848	< 65.91	Swift-XRT
	56862.039	56862.039	< 156.22	Swift-XRT
	56868.172	56868.172	< 141.67	Swift-XRT
	56998.742	56999.211	< 6.21	Swift-XRT
	57616.012	57616.488	< 6.55	Swift-XRT
LSQ14fxj	56959.477	56959.492	< 47.59	Swift-XRT
	56960.156	56960.172	< 70.61	Swift-XRT
	56962.812	56962.828	< 39.40	Swift-XRT
	56964.539	56964.555	< 28.48	Swift-XRT
	56966.070	56966.086	< 42.13	Swift-XRT
	56997.109	56998.000	< 5.27	Swift-XRT
	57033.000	57034.406	< 10.73	Swift-XRT
	57036.523	57036.930	< 16.23	Swift-XRT
	57039.527	57039.668	< 61.25	Swift-XRT
	57051.969	57051.969	< 440.81	Swift-XRT
LSQ14mo	57055.383	57055.383	< 252.78	Swift-XRT
	57189.172	57189.992	< 4.76	Swift-XRT
	56688.758	56690.039	< 32.72	Swift-XRT
	56692.023	56692.039	< 53.38	Swift-XRT
	56693.039	56693.055	< 55.55	Swift-XRT
	56697.961	56697.977	< 49.91	Swift-XRT
	56699.711	56699.727	< 63.80	Swift-XRT
	56754.113	56754.676	< 4.51	Swift-XRT
	56836.836	56836.852	< 57.29	Swift-XRT
	56837.098	56838.371	< 14.19	Swift-XRT
PS1-14bj	56839.023	56839.977	< 18.18	Swift-XRT
	56846.293	56846.371	< 22.74	Swift-XRT
	56953.039	56953.586	< 19.53	Swift-XRT
	57052.594	57054.000	< 8.59	Swift-XRT
	57054.398	57055.742	< 22.96	Swift-XRT
	57063.781	57063.789	< 78.55	Swift-XRT
	57586.496	57586.496	< 442.68	Swift-XRT
	57593.207	57593.355	< 22.96	Swift-XRT
	56817.145	56817.590	< 1.96	XMM
	56968.219	56968.625	< 0.33	XMM
DES15C3hav	57551.984	57552.453	< 7.81	Swift-XRT
	57555.062	57555.391	< 22.96	Swift-XRT
DES15S2nr	57644.625	57644.773	< 11.87	Swift-XRT
	57290.133	57290.148	< 33.39	Swift-XRT
	57290.555	57290.555	< 111.70	Swift-XRT
	57291.328	57291.406	< 15.69	Swift-XRT

TABLE 5 — *Continued*

SN	$t_{START}$ (MJD)	$t_{STOP}$ (MJD)	Unabsorbed Flux (0.3–10 keV) ( $10^{-14} \text{ erg s}^{-1} \text{ cm}^{-2}$ )	Instrument
	57293.461	57294.000	< 12.48	Swift-XRT
	57298.133	57299.000	< 11.71	Swift-XRT
	57303.703	57303.984	< 12.68	Swift-XRT
	57308.035	57308.691	< 7.27	Swift-XRT
	57334.172	57334.172	< 337.41	Swift-XRT
	57336.359	57336.969	< 4.83	Swift-XRT
	57433.484	57433.953	< 7.65	Swift-XRT
	57645.023	57645.227	< 9.82	Swift-XRT
OGLE15qz	57351.859	57351.922	< 62.99	Swift-XRT
OGLE15sd	57364.891	57364.930	< 619.08	Swift-XRT
	57364.953	57365.062	< 56.75	Swift-XRT
SN2015bn/PS15ae	57072.289	57072.508	< 6.68	Swift-XRT
	57073.562	57074.781	< 13.44	Swift-XRT
	57075.352	57076.977	< 65.29	Swift-XRT
	57078.289	57078.367	< 27.40	Swift-XRT
	57080.484	57080.562	< 31.44	Swift-XRT
	57082.277	57083.957	< 32.08	Swift-XRT
	57084.344	57084.359	< 25.66	Swift-XRT
	57089.938	57090.016	< 30.98	Swift-XRT
	57090.402	57090.551	< 15.02	Swift-XRT
	57093.594	57093.938	< 25.59	Swift-XRT
	57098.984	57099.000	< 47.93	Swift-XRT
	57100.984	57100.984	< 2411.59	Swift-XRT
	57102.578	57102.719	< 30.57	Swift-XRT
	57106.836	57106.914	< 35.63	Swift-XRT
	57110.695	57110.695	< 110.20	Swift-XRT
	57111.430	57111.578	< 15.17	Swift-XRT
	57118.352	57118.500	< 30.49	Swift-XRT
	57120.750	57120.891	< 22.87	Swift-XRT
	57122.008	57122.148	< 48.68	Swift-XRT
	57122.281	57123.289	< 14.57	Swift-XRT
	57128.594	57128.672	< 16.11	Swift-XRT
	57131.254	57131.801	< 43.78	Swift-XRT
	57131.258	57131.812	< 8.57	Swift-XRT
	57136.312	57136.320	< 48.68	Swift-XRT
	57144.305	57144.648	< 14.87	Swift-XRT
	57151.152	57151.230	< 13.93	Swift-XRT
	57160.594	57160.672	< 18.12	Swift-XRT
	57166.250	57166.453	< 15.47	Swift-XRT
	57172.375	57172.453	< 19.21	Swift-XRT
	57185.141	57185.281	< 12.00	Swift-XRT
	57206.758	57206.906	< 17.66	Swift-XRT
	57231.367	57231.430	< 26.15	Swift-XRT
	57232.297	57232.453	< 10.98	Swift-XRT
	57330.652	57330.793	< 28.42	Swift-XRT
	57335.781	57335.797	< 28.76	Swift-XRT
	57357.648	57357.805	< 20.15	Swift-XRT
	57390.031	57390.648	< 6.19	Swift-XRT
	57449.070	57449.930	< 17.47	Swift-XRT
	57450.320	57450.867	< 30.42	Swift-XRT
	57455.504	57455.574	< 58.12	Swift-XRT
	57456.766	57456.766	< 223.42	Swift-XRT
	57457.359	57457.375	< 38.87	Swift-XRT
	57572.016	57572.086	< 28.15	Swift-XRT
	57573.215	57574.215	< 11.06	Swift-XRT
	57576.141	57576.336	< 75.48	Swift-XRT
	57580.852	57580.930	< 26.38	Swift-XRT
	57582.246	57582.715	< 23.89	Swift-XRT
	57584.633	57584.836	< 30.38	Swift-XRT
	57586.633	57586.836	< 29.63	Swift-XRT
	57588.227	57588.227	< 95.10	Swift-XRT
	57590.023	57590.227	< 28.23	Swift-XRT
	57591.348	57592.355	< 19.17	Swift-XRT
	57174.250	57174.547	< 0.98	XMM
	57374.953	57375.250	< 0.53	XMM
PS16op	57407.062	57407.594	< 13.55	Swift-XRT
SN2016ard/PS16aqv	57456.320	57456.523	< 8.53	Swift-XRT
	57460.578	57460.922	< 14.08	Swift-XRT
	57464.559	57464.965	< 10.55	Swift-XRT
	57467.953	57468.891	< 9.40	Swift-XRT
	57471.016	57471.141	< 21.42	Swift-XRT
	57476.062	57476.992	< 13.37	Swift-XRT
	57477.109	57477.797	< 37.29	Swift-XRT
	57480.500	57480.719	< 10.08	Swift-XRT
	57484.621	57484.902	< 9.04	Swift-XRT
	57488.027	57488.895	< 16.34	Swift-XRT

TABLE 5 — *Continued*

SN	$t_{START}$ (MJD)	$t_{STOP}$ (MJD)	Unabsorbed Flux (0.3-10 keV) ( $10^{-14} \text{ erg s}^{-1} \text{ cm}^{-2}$ )	Instrument
	57492.609	57492.688	< 30.15	Swift-XRT
	57493.328	57493.406	< 29.75	Swift-XRT
	57496.188	57496.531	< 24.71	Swift-XRT
	57497.250	57497.672	< 29.08	Swift-XRT
	57548.047	57548.695	< 22.61	Swift-XRT
	57549.555	57549.711	< 16.82	Swift-XRT